

1 **RESEARCH ARTICLE**

2
3 **Single-Organelle Quantification Reveals Stoichiometric and Structural**
4 **Variability of Carboxysomes Dependent on the Environment**

5
6 **Yaqi Sun^{1†}, Adam J. M. Wollman^{2†}, Fang Huang¹, Mark C. Leake^{2*}, Lu-Ning Liu^{1*}**

7
8 ¹ Institute of Integrative Biology, University of Liverpool, Liverpool L69 7ZB, United Kingdom

9 ² Biological Physical Sciences Institute, Departments of Physics and Biology, University of York, YO10
10 5DD, United Kingdom

11
12 [†] These authors contributed equally to this work.

13 * Corresponding authors:

14 **Mark C. Leake**, Tel.: +44 (0)190 432 2697, Email: mark.leake@york.ac.uk

15 **Lu-Ning Liu**, Tel.: +44 (0)151 795 4426, Email: luning.liu@liverpool.ac.uk

16
17 **Short title:** Carboxysome protein stoichiometry and variability

18
19 **One Sentence Summary:** Determination of absolute protein stoichiometry reveals the organizational
20 variability of carboxysomes in response to microenvironmental changes

21
22 The authors responsible for distribution of materials integral to the findings presented in this article in
23 accordance with the policy described in the Instructions for Author (www.plantcell.org) is: Lu-Ning Liu
24 (luning.liu@liverpool.ac.uk).

25
26 **ABSTRACT**

27 The carboxysome is a complex, proteinaceous organelle that plays essential roles in carbon
28 assimilation in cyanobacteria and chemoautotrophs. It comprises hundreds of protein homologs that
29 self-assemble in space to form an icosahedral structure. Despite its significance in enhancing CO₂
30 fixation and potentials in bioengineering applications, the formation of carboxysomes and their
31 structural composition, stoichiometry and adaptation to cope with environmental changes remain
32 unclear. Here we use live-cell single-molecule fluorescence microscopy, coupled with confocal and
33 electron microscopy, to decipher the absolute protein stoichiometry and organizational variability of
34 single β-carboxysomes in the model cyanobacterium *Synechococcus elongatus* PCC7942. We
35 determine the physiological abundance of individual building blocks within the icosahedral
36 carboxysome. We further find that the protein stoichiometry, diameter, localization and mobility
37 patterns of carboxysomes in cells depend sensitively on the microenvironmental levels of CO₂ and
38 light intensity during cell growth, revealing cellular strategies of dynamic regulation. These findings,
39 also applicable to other bacterial microcompartments and macromolecular self-assembling systems,
40 advance our knowledge of the principles that mediate carboxysome formation and structural
41 modulation. It will empower rational design and construction of entire functional metabolic factories in
42 heterologous organisms, for example crop plants, to boost photosynthesis and agricultural productivity.

43
44 **Keywords**

45 Bacterial microcompartment, carboxysome, protein stoichiometry, self-assembly, single-molecule
46 fluorescence imaging, structural flexibility

INTRODUCTION

Organelle formation and compartmentalization within eukaryotic and prokaryotic cells provide the structural foundation for segmentation and modulation of metabolic reactions in space and time. Bacterial microcompartments (BMCs) are self-assembling organelles widespread among bacterial phyla (Axen et al., 2014). By physically sequestering specific enzymes key for metabolic processes from the cytosol, these organelles play important roles in CO₂ fixation, pathogenesis, and microbial ecology (Yeates et al., 2010; Bobik et al., 2015). According to their physiological roles, three types of BMCs have been characterized: the carboxysomes for CO₂ fixation, the PDU microcompartments for 1,2-propanediol utilization, and the EUT microcompartments for ethanolamine utilization.

The common features of various BMCs are that they are ensembles composed of purely protein constituents and comprise an icosahedral single-layer shell that encases the catalytic enzyme core. This proteinaceous shell, structurally resembling virus capsids, is self-assembled from several thousand polypeptides of multiple protein paralogs that form hexagons, pentagons and trimers (Kerfeld and Erbilgin, 2015; Sutter et al., 2016; Faulkner et al., 2017). The highly-ordered shell architecture functions as a physical barrier that concentrates and protects enzymes, as well as selectively gating the passage of substrates and products of enzymatic reactions (Yeates et al., 2010; Bobik et al., 2015).

Carboxysomes serve as the key CO₂-fixing machinery in all cyanobacteria and some chemoautotrophs. The primary carboxylating enzymes, ribulose-1,5-bisphosphate carboxylase oxygenase (Rubisco) (Rae et al., 2013), are encapsulated by the carboxysome shell that facilitates the diffusion of HCO₃⁻ and probably reduces CO₂ leakage into the cytosol (Dou et al., 2008). Based on the form of enclosed Rubisco, carboxysomes can be categorized into two different classes, α -carboxysomes and β -carboxysomes (Rae et al., 2013; Kerfeld and Melnicki, 2016). The β -carboxysomes in the cyanobacterium *Synechococcus elongatus* PCC7942 (Syn7942) have been extensively characterized as the model carboxysomes. The shell of β -carboxysomes from Syn7942 is composed of the hexameric proteins CcmK2, CcmK3 and CcmK4 that form predominately the shell facets (Kerfeld et al., 2005), the pentameric protein CcmL that caps the vertices of the polyhedron (Tanaka et al., 2008), as well as the trimeric proteins CcmO and CcmP (Cai et al., 2013; Larsson et al., 2017). The core enzymes of β -carboxysomes consist of a paracrystalline arrangement of plant-type

Rubisco (comprising the large and small subunits RbcL and RbcS) and β -carbonic anhydrase (β -CA, encoded by the *ccaA* gene). The colocalized β -CA dehydrates HCO_3^- to CO_2 and creates a CO_2 -rich environment in the carboxysome lumen to favor the carboxylation of Rubisco. In addition, CcmM and CcmN function as “linker” proteins to promote Rubisco packing and shell-interior association (Kinney et al., 2012). CcmM in the β -carboxysome appears as two isoforms, a 35-kDa truncated CcmM35 and a full-length 58-kDa CcmM58 (Long et al., 2007; Long et al., 2010; Long et al., 2011). CcmM35 contains three Rubisco small subunit-like (SSU) domains that interact with Rubisco (Hagen et al., 2018b; Wang et al., 2019), whereas CcmM58 has an N-terminal γ -CA-like domain in addition to the SSU domains and recruits CcaA to the shell. RbcX is recognized as a chaperonin-like protein for Rubisco assembly (Emlyn-Jones et al., 2006; Saschenbrecker et al., 2007; Occhialini et al., 2016); it has been recently revealed to serve as one component of the carboxysome and play roles in mediating carboxysome assembly and subcellular distribution (Huang et al., 2019).

Understanding the physiological composition and assembly principles of carboxysome building blocks is of key importance not solely to unravel the underlying molecular mechanisms of carboxysome formation and biological functions, but also for heterologously engineering and modulating functional CO_2 -fixing organelles to supercharge photosynthetic carbon fixation in synthetic biology applications. Previous estimations of the carboxysome protein stoichiometry from either the whole cell lysates or the isolated forms using immunoblot and mass spectrometry illustrated the relative abundance of carboxysome proteins (Long et al., 2005; Long et al., 2011; Rae et al., 2012; Faulkner et al., 2017). Moreover, it was revealed that carboxysome biosynthesis in Syn7942 is highly dependent upon environmental conditions during cell growth, such as light intensity (Sun et al., 2016) and CO_2 availability (McKay et al., 1993; Harano et al., 2003; Woodger et al., 2003; Whitehead et al., 2014). The exact stoichiometry of all building components in the functional carboxysome and how carboxysomes manipulate their compositions, organizations and functions to cope with environmental changes have remained elusive.

Here, we construct a series of Syn7942 mutants with individual components of carboxysomes functionally tagged with the bright and fast-maturing enhanced yellow fluorescent protein (YFP) and report the *in vivo* characterization of protein stoichiometry of carboxysomes at the single-organelle level, using real-time single-molecule fluorescence microscopy, confocal and

114 electron microscopy combined with a suite of biochemical and genetic assays. Quantification
115 of the protein stoichiometry of β -carboxysomes in Syn7942 grown under different conditions
116 demonstrates the organizational flexibility of β -carboxysomes, and their ability to modulate
117 functions towards local alterations of CO₂ levels and light intensity during cell growth, as well
118 as the regulation of the spatial localization and mobility of β -carboxysomes in the cell. This
119 study provides fundamental insight into the formation and structural plasticity of
120 carboxysomes and their dynamic organization towards environmental changes, which could
121 be extended to other BMCs and macromolecular systems. A deeper understanding of the
122 protein composition and structure of carboxysomes will inform strategies for rational design
123 and engineering of functional and adjustable metabolic modules towards biotechnological
124 applications.

125

126

RESULTS

Protein stoichiometry of functional carboxysomes at the single-organelle level

We constructed ten Syn7942 strains expressing individual β -carboxysome proteins (CcmK3, CcmK4, CcmK2, CcmL, CcmM, CcmN, RbcL, RbcS, CcaA, RbcX) fused with YFP at their C-termini individually (Supplemental Figure 1). Fluorescence tagging at the native chromosomal locus under the control of their native promoters ensures expression of the fluorescently-tagged proteins in context and at physiological levels (Sun et al., 2016). Eight of these strains, in which YFP was fused to CcmK3, CcmK4, CcmL, CcmM, CcmN, RbcS, CcaA, and RbcX respectively, are fully segregated (Supplemental Figures 1C and 2) and exhibit wild-type levels of cell size, growth and carbon fixation within experimental error (Supplemental Table 1), consistent with previous observations (Savage et al., 2010; Cameron et al., 2013; Sun et al., 2016; Faulkner et al., 2017; Huang et al., 2019).

By contrast, RbcL-YFP and CcmK2-YFP strains are only partially segregated, in agreement with previous studies (Savage et al., 2010; Cameron et al., 2013; Sun et al., 2016). Through immunoblot analysis using anti-fluorescence protein, anti-RbcL and anti-CcmK2 antibodies (Supplemental Figure 2B), we estimate that 29.2 ± 7.1 % (mean \pm standard deviation (SD), $n = 4$) of total RbcL and 6.0 ± 0.7 % ($n = 3$) of total CcmK2 were tagged with YFP in RbcL-YFP and CcmK2-YFP strains. Nevertheless, we excluded the stoichiometric quantification of RbcL and CcmK2 in this study, in view of the partial segregation which could result in quantification inaccuracy.

We used single-molecule Slimfield microscopy (Plank et al., 2009) to visualize individual carboxysomes that were fused with YFP (Figure 1, Supplemental Figure 3). This technique allows detection of fluorescently-labelled proteins with millisecond sampling, enabling real-time tracking of rapid protein dynamics inside living cells, exploited previously to study functional proteins involved in bacterial DNA replication and remodeling (Reyes-Lamothe et al., 2010; Badrinarayanan et al., 2012), gene regulation in budding yeast cells (Wollman et al., 2017; Leake, 2018), bacterial cell division (Lund et al., 2018), and chemokine signaling in lymph nodes (Miller et al., 2018). Our prior measurements using relatively fast-maturing fluorescent proteins such as YFP suggest that less than 15% of fluorescent proteins are likely to be in a non-fluorescent immature state (Leake et al., 2008; Shashkova et al., 2018).

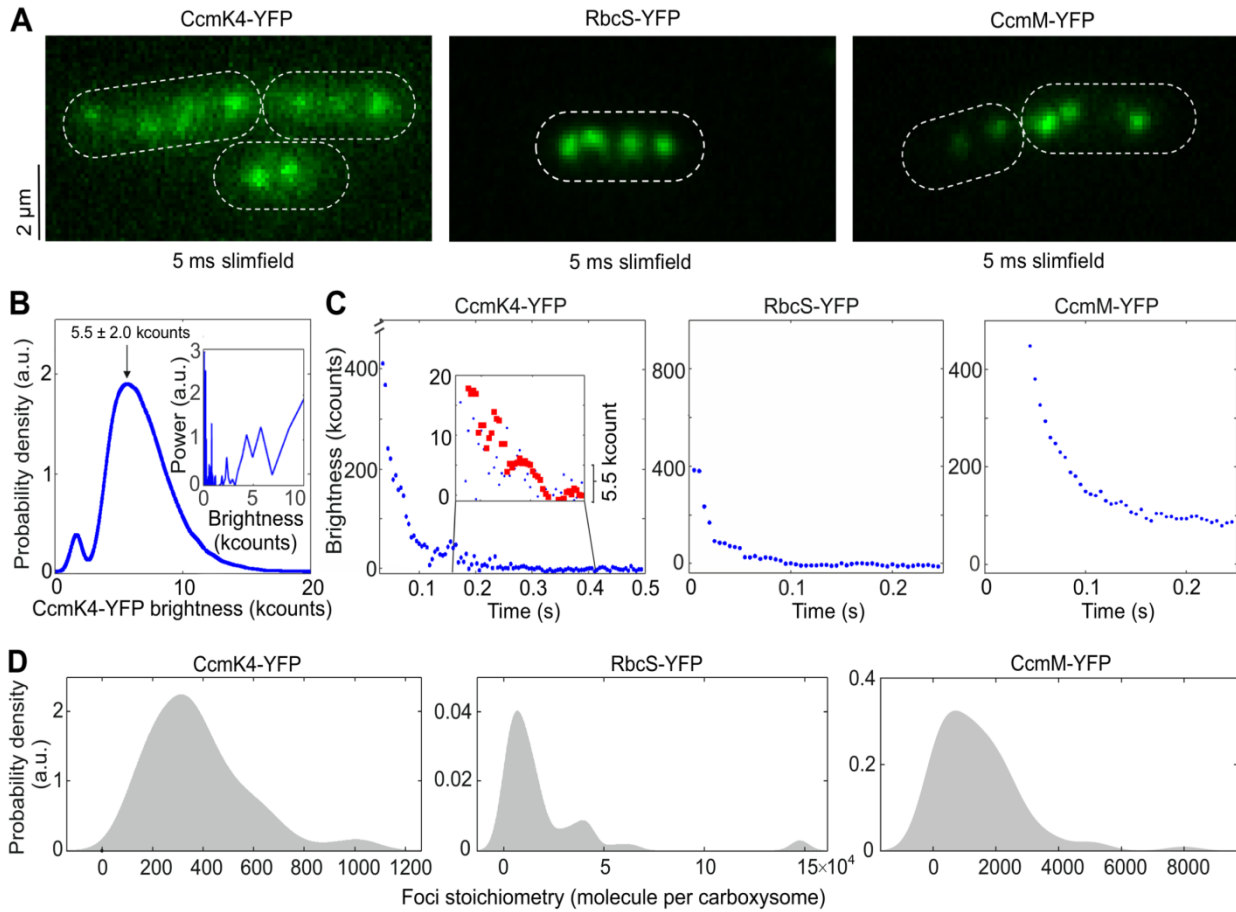


Figure 1. Slimfield quantification of cells grown under ambient air/moderate light Air/ML condition.

(A) Averaged Slimfield images of YFP fluorescence (green) over 5 frames of strains expressing shell component CcmK4-YFP, the interior enzyme RbcS-YFP and the shell-interior linker protein CcmM-YFP. White dash lines indicate cell body outlines.

(B) Distribution of automatically detected foci intensity from the end of the photobleaching, corresponding to the characteristic intensity of *in vivo* YFP. Inset shows the Fourier spectrum of ‘overtracked’ foci, tracked beyond photobleaching, showing a peak at the characteristic intensity.

(C) Representative fluorescence photobleaching tracked at ultra-fast speed. The CcmK4 plot shows an inset ‘zoomed in’ on lower intensity range with step-preserving Chung-Kennedy filtered data in red, with individual photobleaching steps clearly visible at the characteristic intensity. Brightness (kcounts), counts measured per camera pixel multiplied by 1,000.

(D) Distribution of YFP copy number detected for individual carboxysomes in corresponding mutants, rendered as kernel density estimates using standard kernel width. Heterogeneity of contents was observed, also a “preferable” copy number, represented by kernel density peak values could be determined. Statistics of copy numbers (Peak value \pm HWHM) are listed in Table 1 for ML conditions. The corresponding Slimfield images and histogram for complete strain sets are shown in Supplemental Figure 3.

160 Figure 1A shows the Slimfield images of three representative Syn7942 strains RbcS-YFP,
161 CcmK4-YFP and CcmM-YFP that grow under ambient air and moderate light (hereafter

denoted Air/ML), to determine the protein stoichiometry from different carboxysome structural domains. Single carboxysomes are detected as distinct fluorescent foci in cells of the YFP-fused strains (Figure 1A, Supplemental Figure 3), whose sigma width is approximately 250 nm ($n = 100$), comparable to the diffraction-limited point spread function width of our imaging system. We use the number of YFP molecules per fluorescent focus as an indicator of the stoichiometry of the fluorescently-labelled protein subunits in each individual carboxysomes, which we determined by quantifying step-wise photobleaching of the fluorescent tag during the Slimfield laser excitation process (Figures 1B to 1C, Table 1) using a combination of Fourier spectral analysis and edge-preserving filtration of the raw data (Leake et al., 2003; Leake et al., 2004; Leake et al., 2006) (see details in Materials and Methods). The resulting broad distributions of protein stoichiometry, rendered as kernel density estimates, suggest a variable content of individual components per carboxysome (Figure 1D), indicative of the structural heterogeneity of β -carboxysomes. The modal average stoichiometry of each protein subunit per carboxysome was defined by the measured peak from each distribution of the raw stoichiometric data (Figure 1D, Supplemental Figure 3), after subtracting the background fluorescence distribution, primarily from chlorophylls, which was determined from the WT cells (Supplemental Figure 4).

In the β -carboxysome synthesized in cells grown under Air/ML, Rubisco enzymes are the predominant components, as indicated by the RbcS content (Table 1). CcmM is the second most abundant element; there are over 700 copies of CcmM molecules per β -carboxysome. In addition, the CcmK4 content is greater than that of CcmK3 by a factor of 3.8. CcmL, CcmN, CcaA and RbcX are the minor components in the β -carboxysome. Our results reveal that there are 37 CcmL subunits per carboxysome, with the raw stoichiometry distribution showing some indications of peaks at multiples of ~ 5 molecules indicative of multiples of CcmL pentamers (Supplemental Figure 4C), consistent with the atomic structure of CcmL (Tanaka et al., 2008). A modal average of 37 CcmL molecules thus suggests that a single carboxysome contains an average of 7.4 CcmL pentamers, less than the 12 CcmL pentamers that were postulated to occupy all the vertices of the icosahedral shell (Bobik et al., 2015; Kerfeld et al., 2018). It is feasible that not all vertices of the carboxysome structure are capped by CcmL pentamers, as BMC shells deficient in pentamers could still be formed without notable structural variations (Cai et al., 2009; Lassila et al., 2014; Hagen et al., 2018a).

194 Our study represents a direct characterization of protein stoichiometry at the level of single
195 functional carboxysomes in their native cellular environment.

196

197 As a control, we fused RbcL with mYPet, a monomeric-optimized variant of YFP. The RbcL-
198 YFP and RbcL-mYPet cells show no significant difference in the subcellular distribution of
199 carboxysomes as well as cell doubling times and carbon fixation (Supplemental Figure 5),
200 demonstrating that there are no measurable artefacts due to putative effects of dimerization of
201 the YFP tag.

202

203 We also examined the relative abundance of individual carboxysome proteins in the YFP-
204 fusion Syn7942 strains in cell lysates, using immunoblot probing with an anti-fluorescent
205 protein antibody (Supplemental Figure 2A, Supplemental Table 2). To compare with the
206 stoichiometry obtained from Slimfield, we normalized the abundance of carboxysome proteins
207 estimated from immunoblot analysis, using the RbcS content per carboxysome determined by
208 Slimfield. It appears that the content of β -carboxysome proteins determined by
209 immunoblotting is generally greater than that within the carboxysome characterized by
210 Slimfield. Despite the potential effects caused by YFP fusion, this could suggest the presence
211 of a “storage pool” of carboxysome proteins located in the cytoplasm that are involved in the
212 biogenesis, maturation and turnover of carboxysomes. The ratio of RbcL/S detected from cell
213 lysates fraction is about 8:5.8 ($n = 4$) (Supplemental Table 2), in line with previous results
214 (Long et al., 2011) but distinct from the *in vitro* reconstitution observations (Ryan et al., 2018;
215 Wang et al., 2019).

216

217 **Stoichiometry of carboxysome proteins exhibit a dependence on the** 218 **microenvironment conditions of live cells**

219 Our previous study showed that the content and spatial positioning of β -carboxysomes in
220 Syn7942 are dependent upon light intensity during cell growth, revealing the physiological
221 regulation of carboxysome biosynthesis (Sun et al., 2016). Whether the stoichiometry of
222 different components in the carboxysome structure changes in response to fluctuations in
223 environmental conditions is unknown. Here we addressed this question by taking advantage
224 of the far greater throughput of confocal microscopy compared to Slimfield, whilst still using
225 the single-molecule precise Slimfield data as a calibration to convert the intensity of detected
226 foci from confocal images into estimates for absolute numbers of stoichiometry. We achieved

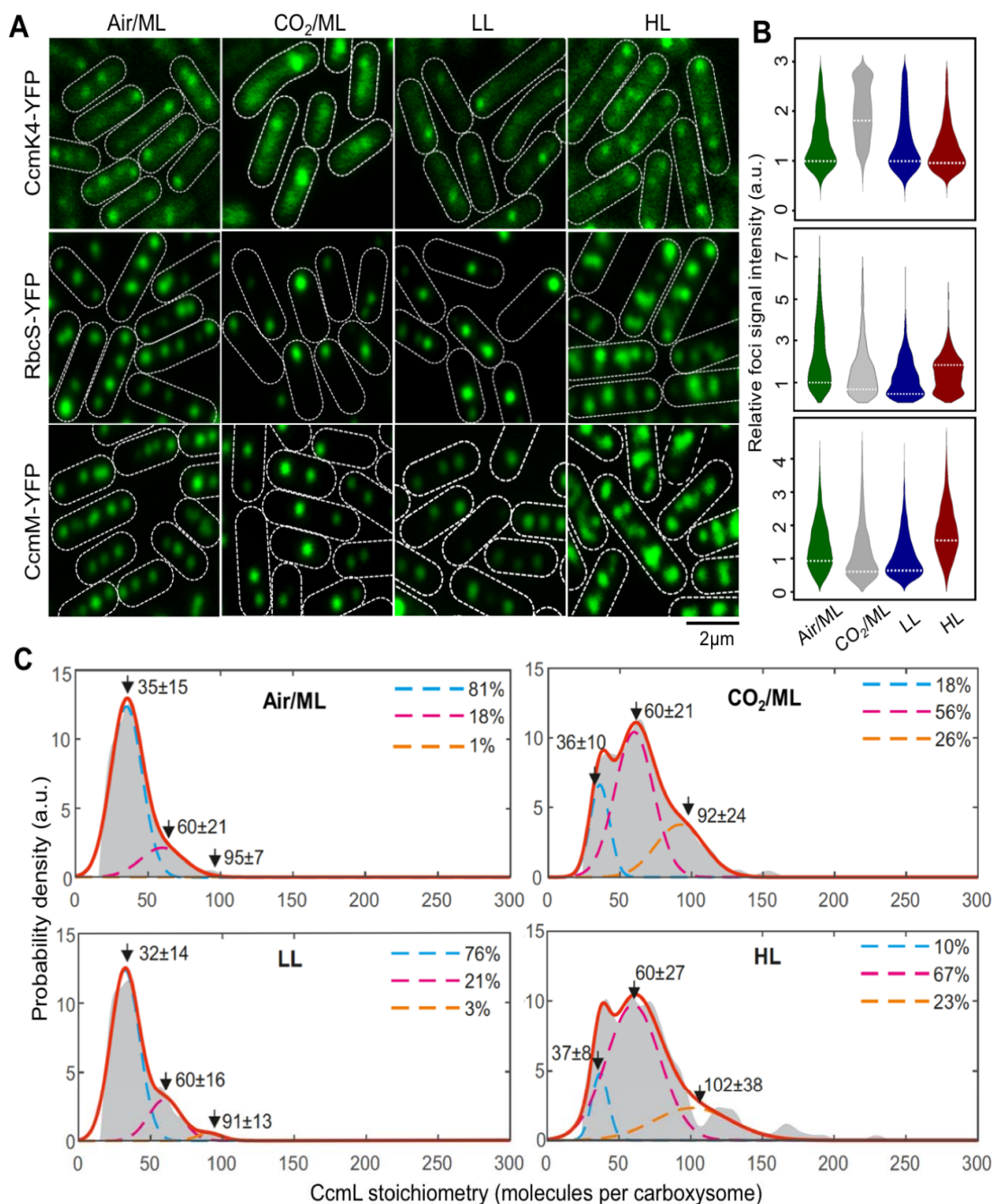


Figure 2. Relative protein quantification of CcmK4, RbcS and CcmM in the carboxysome under different CO₂ levels and light intensities using confocal microscopy.

(A) Confocal images of CcmK4-YFP, RbcS-YFP and CcmM-YFP strains under Air/ML, CO₂/ML, LL and HL. Fluorescence foci (green) indicate carboxysomes and cell borders were outlined by white dashed lines. Scale bar indicates 2 μ m.

(B) Violin plot of carboxysome intensities under Air/ML, CO₂/ML, LL and HL, normalized to kernel density ML peak values (peaks marked by white dash lines).

(C) Kernel density estimates of CcmL carboxysome copy number grown under Air/ML, CO₂, LL and HL detected by Slimfield and corrected for chlorophyll. Triple Gaussian fits are indicated as colored dashed lines with summed fit in red. The percentage in each Gaussian is indicated aside.

228 obtained from confocal imaging with the peak value of the measured Slimfield foci
229 stoichiometry distribution for the equivalent cell strain under Air/ML. This approach allows us
230 to generate a conversion factor which we then applied to subsequent confocal data acquired
231 under lower light (LL), higher light (HL) and ML with the air supplemented by 3% CO₂, and to
232 estimate relative changes in the stoichiometry of carboxysome building components using
233 large numbers of cells, without the need to obtain separate Slimfield datasets for each
234 condition (Figure 2, Supplemental Figures 6 to 8).

235

236 Figure 2A shows confocal fluorescence images of RbcS-YFP, CcmK4-YFP, and CcmM-YFP
237 strains grown under Air/ML, 3% CO₂ (CO₂/ML), LL and HL. The confocal images reveal
238 classic patterns of cellular localization of carboxysomes similar to those observed with
239 Slimfield microscopy (Supplemental Figure 6). We analyzed the confocal images to detect
240 carboxysome fluorescent foci within the cells and quantify their fluorescence intensities
241 (Figure 2B, Supplemental Figures 7 and 8). We find that the number of carboxysomes per cell
242 is dependent on growth conditions: it is reduced under CO₂/ML in contrast to Air/ML, whereas
243 HL increases the abundance of β -carboxysomes (Supplemental Table 3), consistent with
244 previous findings (Whitehead et al., 2014; Sun et al., 2016). The slightly different
245 carboxysome contents estimated in individual YFP-fused strains might suggest potential
246 mechanisms of the cells that tune carboxysome organization. As a common feature, the
247 abundance of all the proteins in the β -carboxysome is apparently modulated under distinct
248 growth conditions. For instance, both RbcS and CcmM have a higher content per
249 carboxysome under HL compared with that under other conditions, whereas the CcmK4
250 content per β -carboxysome increase under 3% CO₂ (Figure 2B). The dependence of
251 carboxysome protein stoichiometry inferred from the peak values of the stoichiometry
252 distributions under different cellular microenvironmental conditions is summarized in Table 1.

253

254 Interestingly, we find that the variation of CcmL abundance per carboxysome rises with
255 increasing light illumination and CO₂ availability (Figure 2C). The measured stoichiometry
256 distribution of CcmL pentamers suggests the presence of three populations: (I) carboxysomes
257 with < 60 CcmL subunits (in the range of 32-37); (II) carboxysomes with 60 CcmL subunits,
258 consistent with the expectation that 12 vertices of the icosahedral carboxysome are fully
259 occupied by CcmL pentamers (Tanaka et al., 2008; Rae et al., 2013; Kerfeld et al., 2018); (III)
260 carboxysomes with > 60 CcmL subunits (in the range of 91-102). Using a nearest-neighbor

261 model to estimate the probability for the diffraction-limited optical images of individual
262 carboxysomes in a cell, we find that the Population III carboxysomes represent random
263 overlap of two or more carboxysomes from the Population I and II (Figure 2C). Population I
264 represents a “non-complete capped” state in which not all vertices in the icosahedron are
265 occupied by CcmL pentamers. We find the characteristic stoichiometry of the Population I
266 carboxysomes increases with the enhancement of light intensity during cell growth, from 32
267 CcmL molecules (LL) to 35 (ML) and 37 (HL), with HL having a significantly smaller proportion
268 (23%) of “non-complete capped” carboxysomes compared to ~80% under LL and ML
269 conditions. Supplementing the air with 3% CO₂ under ML similarly results in a substantial
270 decrease in the proportion of “non-complete capped” carboxysomes in the population (18%)
271 comparable to the HL condition in the absence of any supplemental CO₂. These findings
272 suggest a dependence of carboxysome assembly which may allow adaptation towards
273 microenvironmental changes, i.e. the increase in the population of capped carboxysomes in
274 situations which are favorable towards photosynthesis (HL conditions and locally-raised levels
275 of CO₂).

276

277 This finding is also validated by the changes in protein abundance of other carboxysome
278 components under environmental regulation (Table 1, Supplemental Figures 7 and 8). Cells
279 were maintained under different growth conditions prior to microscopy imaging, to ensure
280 their full acclimation. Variations of protein content in carboxysomes under CO₂/ML vs. Air/ML,
281 and HL vs. LL conditions indicate distinct fashions of stoichiometric regulation of
282 carboxysome building blocks (Figure 3, Supplemental Table 4). The abundance of CcmK3
283 and CcmK4, whose encoding genes are distant from the *ccmKLMNO* operon (Sommer et al.,
284 2017), increases under 3% CO₂ and remains relatively constant under HL/LL, contrary to the
285 changes in the abundance of CcmN and CcmM that are located in the *ccm* operon. In
286 addition, the ratio of CcmK4:CcmK3 per carboxysome appear to be relatively constant, in the
287 range of 3.6–4.1 (Supplemental Table 5), indicating the organizational correlation between
288 CcmK3 and CcmK4 within the β -carboxysome structure. We find the rise of CcaA content and
289 reduction of RbcS content under CO₂/ML vs. Air/ML, whereas both increase under HL,
290 suggesting distinct regulation of the two components. It has been recently demonstrated that
291 the putative Rubisco chaperone RbcX is part of the carboxysome and plays roles in mediating
292 carboxysome formation (Huang et al., 2019). The fold changes of RbcX content in each
293 carboxysome under different conditions are close to 1 (Figure 3), probably ascribed to the fact

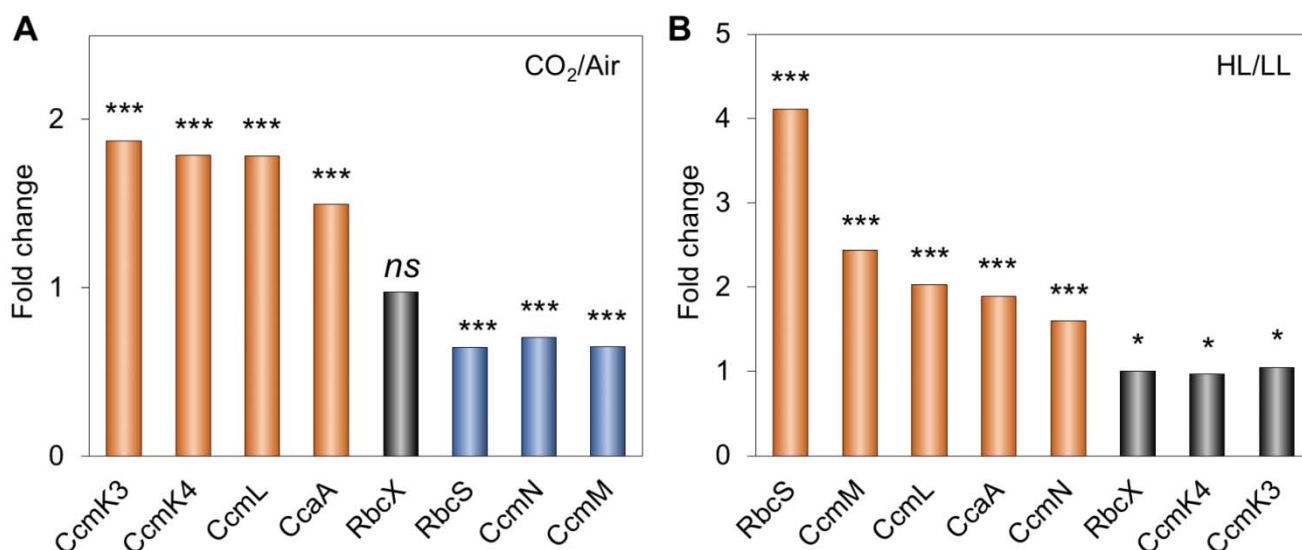


Figure 3. Changes in carboxysome protein stoichiometry by increase in CO_2 levels and light intensity.

(A) Comparison of carboxysome protein stoichiometry under CO_2 treatment. Increase in the CO_2 concentration resulted in the rise of CcmK3, CcmK4, CcaA and CcmL contents and the decline of RbcS, CcmN and CcmM contents.

(B) Comparison of carboxysome protein stoichiometry under light intensity treatment. Increased light intensity led to the elevation of RbcS, CcmM, CcmL, CcaA and CcmN contents, whereas the abundance of RbcX, CcmK3 and CcmK4 contents per carboxysome does not change dramatically.

Man-Whitney U-tests were performed to compare the numbers of functional units of individual carboxysome proteins changed from CO_2/ML to Air/ML (A) and from HL to LL (B). *, $p < 0.05$; ***, $p < 0.005$; ns, $p > 0.05$.

that its encoding gene is distant from the *rubisco* and *ccm* operons in Syn7942. Collectively, these results highlight the highly flexible stoichiometry of individual components within the natural carboxysomes in response to environmental changes.

Variation of carboxysome diameter represents a strategy for manipulating carboxysome activity to adapt to environmental conditions

The change in the protein content per carboxysome signifies the variation of β -carboxysome size and organization among different cell growth conditions. Indeed, electron microscopy (EM) of Syn7942 WT cells substantiates the variable structures of β -carboxysomes in response to the changing environment (Figures 4A and 4B). The average diameter of β -carboxysomes is 192 ± 41 nm ($n = 33$) in Air/ML, 144 ± 24 nm ($n = 25$) in 3% CO_2 , 151 ± 22 nm ($n = 27$) in LL, and 208 ± 28 nm ($n = 51$) in HL (Figure 4B, Supplemental Table 5, Supplemental Figure 9). These results reveal that both the CO_2 level and light intensity can

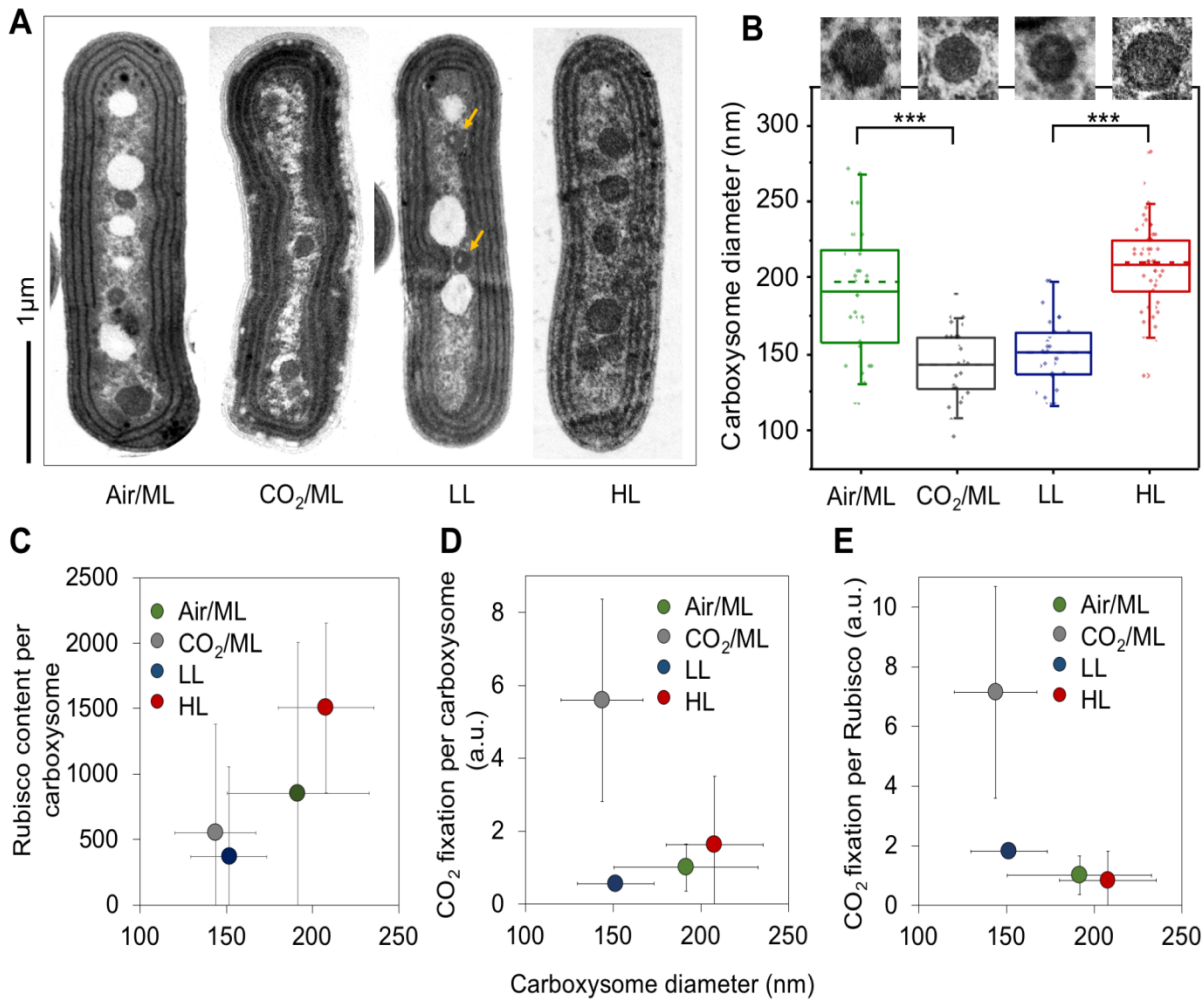


Figure 4. Variations of the carboxysome size and carbon fixation under Air/ML, CO₂, LL and HL.

(A) Thin-section electron microscopy (EM) images showing individual carboxysomes in the Syn7942 WT cells under Air/ML, CO₂, LL and HL treatments. Yellow arrows indicate the carboxysomes with spaces of low protein density under LL. More EM images are shown in Supplemental Figure 9. Scale bar indicates 1 μm.

(B) Changes in the carboxysome diameter under Air/ML, CO₂, LL and HL measured from EM ($n = 33, 25, 27$ and 51 , respectively), with representative carboxysome images depicted above. Dashed lines indicate medians and solid lines indicate means. Differences in the carboxysome diameter are significant between CO₂ and air ($p = 1.92 \times 10^{-14}$) and between LL and HL ($p = 8.29 \times 10^{-7}$), indicated as ***.

(C) Correlation between the carboxysome size and the Rubisco content per carboxysome under Air/ML, CO₂, LL and HL.

(D) Correlation between the carboxysome size and CO₂ fixation per carboxysome.

(E) Correlation between the carboxysome size and CO₂ fixation per Rubisco of the carboxysomes. Carboxysome diameters and CO₂ fixation were present as average \pm SD, whereas the carboxysome total protein content and Rubisco content were shown as Peak value \pm HWHM.

307 result in alternations of carboxysome size (Figure 4B). Larger β -carboxysomes can

308 accommodate more Rubisco enzymes (estimated on the basis of RbcS content) (Figure 4C).
309 An exception is the carboxysomes under LL, which are around 5% larger than the
310 carboxysomes under 3% CO₂ but comprises only 67% of Rubisco per carboxysome under
311 CO₂ (Figure 4C, Supplemental Table 5). EM images reveal that the lumen of β -carboxysomes
312 synthesized under LL often contain regions with low protein density (Figure 4A, arrows;
313 Supplemental Figure 9), 59% for LL (16 out of 27 carboxysomes) compared with 9% for
314 Air/ML (3 out of 33), 12% for CO₂/ML (3 out of 25) and 8% for HL (4 out of 51), which likely
315 accounts for the reduced and uneven Rubisco loading within the β -carboxysome.

316

317 We also find that CO₂-fixing activity per carboxysome increases as the β -carboxysome
318 structure enlarges, which is correlated to strong light intensity during cell growth (Figure 4D),
319 demonstrating the correlation between β -carboxysome structure and function *in vivo*.
320 Moreover, under HL the CO₂-fixation activity per Rubisco of the β -carboxysome declines as
321 the carboxysome size and Rubisco density in the carboxysome lumen increase (Figure 4E,
322 Supplemental Table 5). This may suggest that Rubisco density and local Rubisco packing are
323 important for determining CO₂-fixation activity of individual Rubisco (Supplemental Table 5).
324 Interestingly, the relatively small β -carboxysomes under 3% CO₂ exhibit high CO₂-fixing
325 activities per Rubisco and per carboxysome, compared with β -carboxysomes under other
326 conditions. The enhanced carbon fixation capacity under 3% CO₂ might be correlated with the
327 increase in CcmK3 and CcmK4 content (Figure 3A, Table 1), as it has been shown that
328 depletion of CcmK3/CcmK4 impedes carbon fixation of carboxysomes (Rae et al., 2012).

329

330 **Patterns of spatial localization and diffusion of β -carboxysomes in live cells change** 331 **dynamically depending upon light intensity during growth**

332 The patterns of β -carboxysome localization within the cyanobacterial cells appears to be
333 crucial for carboxysome biogenesis and metabolic function (Savage et al., 2010; Sun et al.,
334 2016). We measured the organizational dynamics of β -carboxysomes with distinct diameters
335 in Syn7942 under different light intensities, using time-lapse confocal fluorescence imaging on
336 the RbcL-YFP Syn7942 strain. Previous studies have shown that tagging of RbcL with
337 fluorescent proteins does not obstruct β -carboxysome assembly and function in Syn7942
338 (Savage et al., 2010; Cameron et al., 2013; Chen et al., 2013; Sun et al., 2016). During time-
339 lapse confocal imaging, we applied illumination on the cell samples, similar to that used for
340 cell growth, in order to maintain cell physiology. We find that the overall mobility of individual

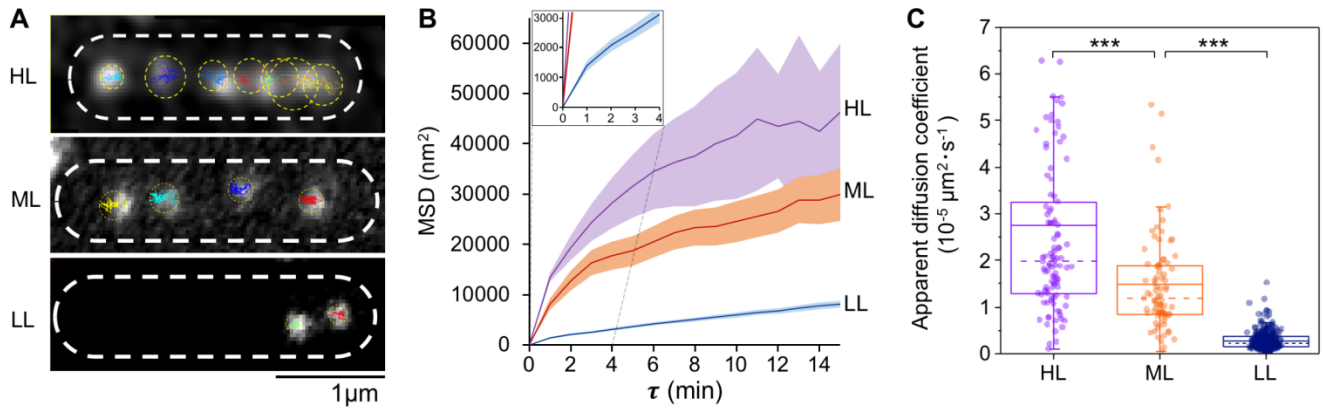


Figure 5. Spatial localization and diffusion dynamics of carboxysomes in Syn7942 cells are dependent on light intensity.

(A) Tracking of carboxysome diffusion in cells grown under HL, ML and LL. Colored lines indicate the diffusion trajectories of each carboxysomes and circles represent the diffusion areas of each carboxysomes over 60 mins. Scale bar indicates 1 μm .

(B) Non-linear MSD (Mean Square Displacement) vs. the time interval (τ) profiles suggest the mobility of carboxysomes in Syn7942 cells grown under HL, ML and LL. Inset, zoom-in view of the MSD profile under LL.

(C) Diffusion coefficient of carboxysomes *in vivo* decreases significantly when the light intensity reduces: $2.76 \pm 2.83 \times 10^{-5} \mu\text{m}^2 \cdot \text{s}^{-1}$ for HL (mean \pm SD, $n = 105$), $1.48 \pm 1.03 \times 10^{-5} \mu\text{m}^2 \cdot \text{s}^{-1}$ for ML ($n = 84$), and $0.28 \pm 0.19 \times 10^{-5} \mu\text{m}^2 \cdot \text{s}^{-1}$ for LL ($n = 336$). $p = 3.05 \times 10^{-5}$ between HL and ML; $p = 2.77 \times 10^{-5}$ between ML and LL, two-tailed Student's t-test).

341 β -carboxysomes within cyanobacterial cells is non-Brownian (Figure 5A, Supplemental Movie
 342 1). Carboxysomes under HL display larger diffusive regions than those under LL. The mean
 343 square displacement (MSD) of tracked carboxysomes increased with the rise of light intensity
 344 (Figure 5B), as did the mean microscopic diffusion coefficient of individual carboxysomes
 345 (Figure 5C): an average diffusion coefficient of $2.76 \pm 2.83 \times 10^{-5} \mu\text{m}^2 \cdot \text{s}^{-1}$ for HL (mean \pm SD,
 346 $n = 105$), $1.48 \pm 1.03 \times 10^{-5} \mu\text{m}^2 \cdot \text{s}^{-1}$ for ML ($n = 84$), and $0.28 \pm 0.19 \times 10^{-5} \mu\text{m}^2 \cdot \text{s}^{-1}$ for LL ($n =$
 347 336). It is interesting that the mobility of carboxysomes does not exhibit typical constrained
 348 diffusion – asymptotic MSD values at higher values of τ (Robson et al., 2013) – but rather
 349 exhibits anomalous diffusion at higher values of τ characterized by a non-linear relation,
 350 which can be observed in the intracellular protein mobility traces of other cellular systems
 351 (Lenn et al., 2008; Wollman et al., 2017). These results indicate the intracellular restrictions,
 352 for example the proposed interactions with the cytoskeletal system (Savage et al., 2010),
 353 McdA and McdB (MacCready et al., 2018) and ParA-mediated chromosome segregation (Jain
 354 et al., 2012), may mediate carboxysome positioning, but do not completely confine the
 355 mobility of carboxysomes. Notably, carboxysomes with a larger diameter (Figure 4) generated

356 under HL present a higher diffusion coefficient compares with carboxysomes with relatively
357 smaller size under ML and LL. However, there is no apparent correlation between the
358 diffusion coefficient of carboxysomes and their size in the same light conditions
359 (Supplemental Figure 10).

360

361

362 **Discussion**

363 Precise quantification of the protein stoichiometry and organizational regulation of
364 carboxysomes provides insight into their assembly principles, structure and function. In this
365 work, we functionally fused fluorescent protein tags to the building blocks in β -carboxysomes
366 and exploited advanced “Physics of Life” technologies, in particular using bespoke single-
367 molecule fluorescence microscopy to count the actual protein stoichiometry of β -
368 carboxysomes in Syn7942 cells, at the single-organelle level. This approach minimizes the
369 ensemble averaging encountered in bulk estimations from proteomic and immunoblot
370 analysis. We characterized the stoichiometric flexibility of carboxysome proteins within
371 individual polyhedral structures towards environmental variations. Variability of the protein
372 stoichiometry and size of carboxysomes likely provides the structural foundation for the
373 physiological regulation of carboxysome formation and carbon fixation activity. Given the
374 shared structural features of carboxysomes and other BMCs, we believe that this work opens
375 up new opportunities to quantitatively evaluate protein abundance and decipher the formation
376 of all BMC organelles, in both native forms and synthetic variants.

377

378 Despite prior efforts on understanding carboxysome structure and function, the relative
379 stoichiometry of functional carboxysome components in their native cell environment – key
380 information required for reconstituting entire active carboxysome structures in synthetic
381 biology (Fang et al., 2018), was still unclear. The major challenges have been the poor
382 specificity of immunoblots and mass spectrometry, given the homology of carboxysome
383 proteins and the lack of effective purification of intact carboxysomes from host cells, as well
384 as the heterogeneity of carboxysome structures (Long et al., 2005). The previous model of
385 carboxysome protein stoichiometry was based on the total amount of proteins in cell lysates
386 (Long et al., 2011) and does not directly reflect the stoichiometry of carboxysome proteins in
387 the organelle, given the possible free-standing carboxysome components in the cytosol (Dai
388 et al., 2018). We have recently reported the isolation of β -carboxysomes from Syn7942 and
389 the structural and mechanical exploration of the organelles (Faulkner et al., 2017).
390 Interestingly, some components, i.e. CcmO, CcmN, CcmP and RbcX, were not detectable by
391 mass spectrometry in the isolated carboxysomes, likely due to their low content or potential
392 loss of carboxysome components during isolation. Here, as demonstrated, fluorescence
393 tagging and Slimfield and confocal imaging enable single-organelle analysis of the protein
394 stoichiometry of eight β -carboxysome proteins (including RbcX) and their regulation in their

native context, and extends analyses of the assembly and action of carboxysomes. Microscopy imaging of fluorescently-tagged β -carboxysomes has been used to reveal their patterns of cellular localization, biogenesis pathways and light-dependent regulation in Syn7942 (Savage et al., 2010; Cameron et al., 2013; Chen et al., 2013; Sun et al., 2016; Niederhuber et al., 2017; MacCready et al., 2018). Although we cannot completely exclude the potential effects of YFP tags on carboxysome structure, we validate that YFP tagging to most of the structural components does not impede formation of functional carboxysome structures, suggesting the physiological relevance of the determined protein stoichiometry in the carboxysome in the presence of fluorescence tags. This flexibility emphasizes the extraordinary capacity of the carboxysome structure in adjusting their protein stoichiometry and accommodating foreign proteins while maintaining functionality, indicating the possibility of manipulating carboxysome organization in bioengineering for diverse purposes. Exceptionally, fluorescence tagging on CcmP and CcmO does not show normal carboxysome assembly and localization compared to other YFP-tagged strains (Supplemental Figure 11). In this work, therefore, we did not include estimation of the protein abundance of CcmP and CcmO, as well as RbcL and CcmK2 that cannot be fully tagged with YFP.

Numerous studies have described the regulation of carboxysome protein expression at the transcriptional level (McGinn et al., 2003; Woodger et al., 2003; Schwarz et al., 2011). Counting protein abundance of β -carboxysomes at different cell growth conditions enables direct characterization of the stoichiometric plasticity of carboxysome building components in the cells grown under not only the same environmental condition but also a range of various conditions (Figure 6A). Our observations elucidate the size variation of β -carboxysomes in Syn7942 cells grown under distinct environmental conditions (Figure 6B) and adjustable carbon fixation capacities of carboxysomes that may be closely linked to the protein organization and size of carboxysomes. Variations in the diameter of intact carboxysomes, ranging from 90 to 600 nm, have been also shown in previous studies not only in single species but also among distinct species (Shively et al., 1973; Price and Badger, 1991; Iancu et al., 2007; Liberton et al., 2011), suggesting the adaptation strategies exploited by cyanobacteria for regulating their CO₂-fixing machines to survive in diverse niches. It may be related to the environment-sensitive protein-protein interactions that drive protein self-assembly and BMC formation (Faulkner et al., 2019). Moreover, the spatial positioning and mobility of β -carboxysomes in live cells appear to be independent of carboxysome diameter

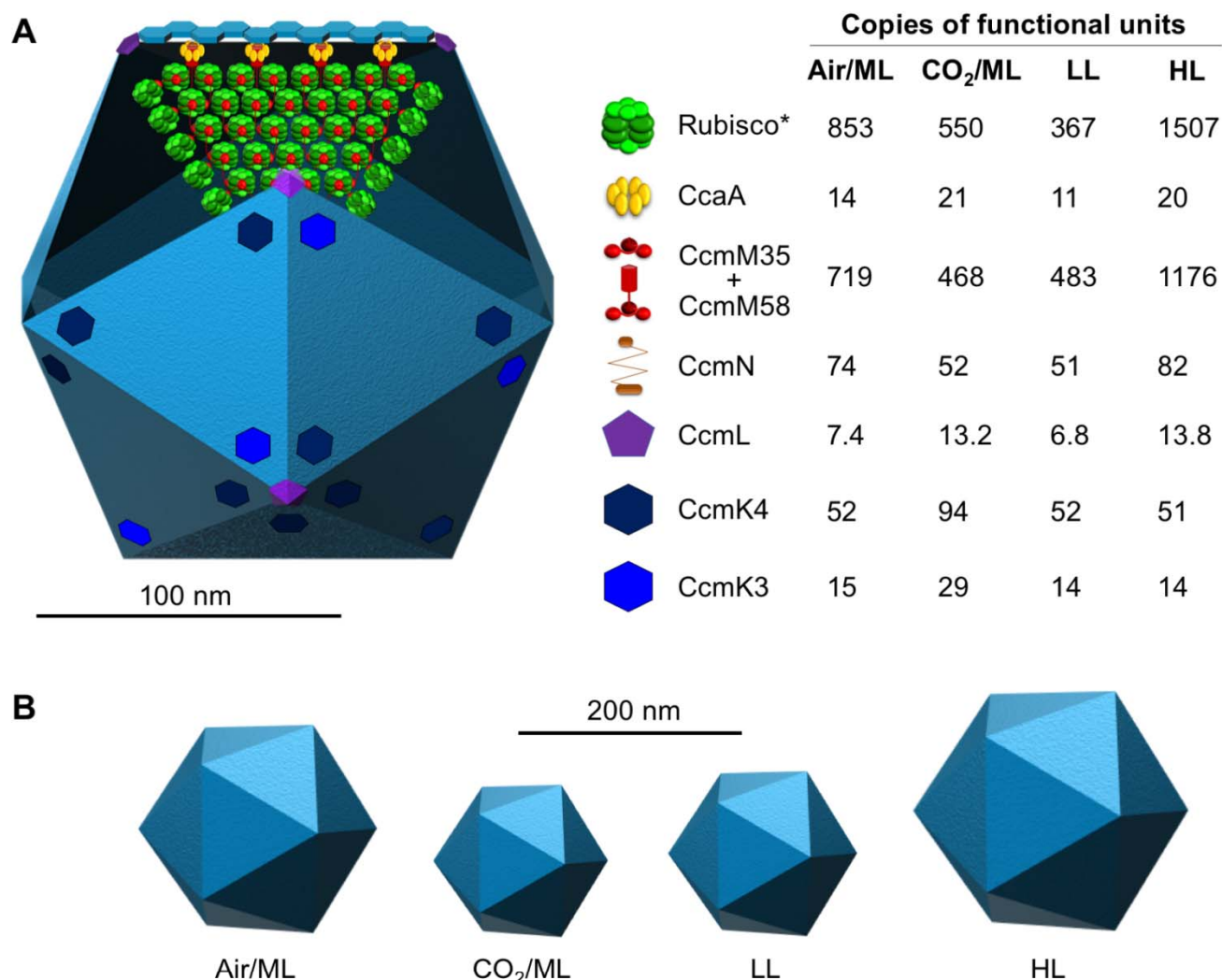


Figure 6. Model of the β -carboxysome structure and protein stoichiometry.

(A) Diagram of an icosahedral carboxysome structure and organization of building components. The stoichiometry of each building component within the carboxysome and its variations in response to changes in CO₂ and light intensity are shown on the right (See also Table 1). *Rubisco content was estimated from RbcS stoichiometry based on the RbcL₈S₈ Rubisco structure. The majority of shell facets shown in light blue is tiled by the major shell protein CcmK2. The total abundance of CcmM58 and CcmM35 was estimated. The components RbcL, CcmK2, CcmO and CcmP were not directly determined in this work and thus are not shown in this model.

(B) The carboxysome diameter is variable in response to changes in the CO₂ level and light intensity.

428 but show a strong dependence to light intensity, suggesting that light-dependent mechanisms
 429 might mediate carboxysome location and diffusion. Carboxysome spacing and partitioning
 430 have been suggested to be driven by different possible mechanisms, such as the cytoskeletal
 431 proteins ParA and MreB (Savage et al., 2010), ParA-mediated chromosome segregation (Jain

et al., 2012) via filament-pull model (Ringgaard et al., 2009) or a diffusion-ratchet model (Vecchiarelli et al., 2013) as well as very recently the McdA and McdB that utilize a Brownian-ratchet mechanism to position carboxysomes (MacCready et al., 2018). Altogether, the organizational flexibility of β -carboxysomes, including modulatable protein stoichiometry, diameter and mobility, may represent the natural strategies for modifying shell permeability and enzyme encapsulation and ensuring structural and functional adaptations dependent on the local cellular environment.

The estimated number of CcmL pentamers per carboxysome could be less than 12, demonstrating explicitly that it is not a prerequisite for CcmL pentamers to occupy all 12 vertices of the icosahedral shell to ensure complete formation of functional carboxysomes. This hypothesis has been validated by previous observations that BMC shells in the absence of pentamers have no significant morphological changes (Cai et al., 2009; Lassila et al., 2014; Hagen et al., 2018a). These “non-complete capped” forms appear to be prevalent among the resultant carboxysomes under Air/ML and LL (Figure 2C), unlike the procarboxysomes (Cameron et al., 2013) or “immature” carboxysomes which are incapable of establishing an oxidative microenvironment for cargo enzymes (Chen et al., 2013). Whether the loss of capping CcmL will create large space within the shell, as a possible mechanism of modulating shell permeability, or will be compensated for by incorporation of other shell proteins, for example the additional CcmP trimers that are speculated to be responsible for permeability, remains to be further investigated. Our results also suggest that carboxysomes could possess a flexible molecular architecture, resonating with the observation of structural “breathing” of virus capsids which has been reported to be key to cope with temperature change (Roivainen et al., 1993; Li et al., 1994). Carboxysomes, though structurally resembling virus capsids, have been shown to be mechanically softer than the P22 virus capsid by a factor of ~ 10 , suggesting greater flexibility of protein-protein interactions within the carboxysome structure (Faulkner et al., 2017). The capping flexibility of pentamers may represent the dynamic nature of shell assembly probably in the second timescale and tunable protein-protein interactions in the shell, as characterized recently (Sutter et al., 2016; Faulkner et al., 2019).

It was proposed that CcmM58 proteins are confined to a subshell layer for linking Rubisco, CcaA and CcmN to the shell, whereas CcmM35 molecules are predominantly located in the core to stimulate Rubisco aggregation (Rae et al., 2013). A recent study revealed that

CcmM35 and CcmM58 display similar distribution profiles in carboxysomes and are both integrated within the core of the carboxysome (Niederhuber et al., 2017). Fluorescence tagging at the protein C-terminus exploited in this work allowed us to only estimate the total amounts of CcmM but not distinguish CcmM35 and CcmM58, which can be addressed by N-terminal labeling of CcmM58 in our future study. Compared with the previous model that was based on protein stoichiometry of cell lysates (Long et al., 2011), our relative quantifications determined under the Air/ML condition show the 4.9-fold and 2.2-fold increases in the ratios of Rubisco/CcmM and Rubisco/CcaA, respectively (Figure 6A, Supplemental Table 5). The discrepancy may be caused by different sampling methods and cultivation conditions.

Based on immunoblot analysis of cell lysates, the previous model has proposed an imbalanced ratio of RbcL to RbcS (~8:5), likely due to the binding of CcmM to Rubisco replacing 3 RbcS subunits (Long et al., 2011). This result was similar to our immunoblot quantification from cell lysates (Supplemental Table 2). Recent studies indicate that CcmM interacts with Rubisco (RbcL₈S₈) at distinct sites, without displacing RbcS (Ryan et al., 2018; Wang et al., 2019). Based on the L₈S₈ ratio and RbcS abundance per carboxysome determined, we estimate that there are approximately 853, 550, 367, and 1507 copies of Rubisco per β -carboxysome under Air/ML, CO₂/ML, LL, and HL, respectively (Figure 6A, Table 1). Even the lowest Rubisco abundance per β -carboxysome (an average diameter of 151 nm) under LL is still greater than the Rubisco abundance per α -carboxysome (an average diameter of 123 nm) (Iancu et al., 2007) by a factor of 1.6. This finding confirms the different interior organization of the two classes of carboxysomes: densely packed with Rubisco forming paracrystalline arrays inside the β -carboxysome (Faulkner et al., 2017) and random packing of Rubisco in the α -carboxysome (Iancu et al., 2007; Iancu et al., 2010). The different interior structures may be ascribed to their distinct biogenesis pathways: biogenesis of β -carboxysomes is initiated from the nucleation of Rubisco and CcmM35 and then the shell encapsulation (Cameron et al., 2013); whereas α -carboxysome assembly appears to start from shell formation (Menon et al., 2008) or a simultaneous shell-interior assembly (Iancu et al., 2010).

While the abundance of most of the structural components varies, the ratio of CcmK4 and CcmK3 is relatively unaffected (ranging from 3.6 to 4.1, Supplemental Table 5) under the tested growth conditions, implying their spatial colocalization within the carboxysome shell

498 (Figure 6A). This is reminiscent of the recent observation that CcmK3 and CcmK4 can form a
499 heterohexameric complex with a 1:2 stoichiometry and further form dodecamers in a pH-
500 dependent manner (Sommer et al., 2019). The *ccmK3* and *ccmK4* genes are located in the
501 same operon that is distant from the *ccm* operon and they may have different expression
502 regulation compared with other carboxysome components (Rae et al., 2012; Sommer et al.,
503 2017). The balanced expression and structural cooperation of CcmK3 and CcmK4 may be
504 crucial for the fine-tuning of carboxysome permeability towards environmental stress.

505

506 Rational design, construction and modulation of bioinspired materials with structural and
507 functional integrity are the major challenges in synthetic biology and protein engineering.
508 Given their self-assembly, modularity and high efficiency in enhancing carbon fixation,
509 carboxysomes have attracted tremendous interest to engineering this CO₂-fixing organelle
510 into other organisms, for example C₃ plants, with the intent of increasing photosynthetic
511 efficiency and crop production (Lin et al., 2014b; Lin et al., 2014a; Occhialini et al., 2016;
512 Long et al., 2018). Recently, we have reported the engineering of functional β -carboxysome
513 structures in *E. coli* – a step towards constructing functional β -carboxysomes in eukaryotic
514 organisms (Fang et al., 2018). Our present study, by evaluating the actual protein
515 stoichiometry and structural variability of native β -carboxysomes, sheds light on the molecular
516 basis underlying the assembly, formation and regulation of functional carboxysomes. It will
517 empower bioengineering to construct BMC-based nano-bioreactors and scaffolds, with
518 functional and tunable compositions and architectures, for metabolic reprogramming and
519 targeted synthetic molecular delivery. A deeper understanding of carboxysome structure and
520 the developed imaging techniques will be broadly extended to other BMCs and
521 macromolecular systems.

522

523

524 **Materials and Methods**

525 **Bacterial strains, growth conditions, light and CO₂ treatment, and generation of** 526 **mutants**

527 Wild-type (WT) and mutant *Synechococcus elongatus* PCC7942 (Syn7942) strains were
528 grown in BG-11 medium in culture flasks with constant shaking or on BG-11 plates containing
529 1.5% (w/v) agar at 30°C. Syn7942 WT and mutants were maintained and grown under
530 different intensities of constant white LED light illumination: 80 $\mu\text{E}\cdot\text{m}^{-2}\cdot\text{s}^{-1}$ as HL (higher light

531 in ambient air), $50 \mu\text{E}\cdot\text{m}^{-2}\cdot\text{s}^{-1}$ as Air/ML (moderate light in ambient air), $10 \mu\text{E}\cdot\text{m}^{-2}\cdot\text{s}^{-1}$ as LL
532 (lower light in ambient air) to ensure full acclimation, respectively. Cultures were grown in air
533 without an additional CO_2 source, except for the CO_2 treatment experiment in which Syn7942
534 cultures in the growth incubators were aerated with 3% CO_2 under moderate light (CO_2 /ML).
535

536 Cultures were constantly diluted with fresh medium to maintain exponential growth phase for
537 the following imaging and biochemical analysis. *Escherichia coli* strains used in this work,
538 DH5a and BW25113, were grown aerobically at 30 or 37°C in Luria-Broth medium. Medium
539 supplements were used, where appropriate, at the following final concentrations: ampicillin
540 $100 \text{ mg}\cdot\text{mL}^{-1}$, chloramphenicol $10 \text{ mg}\cdot\text{mL}^{-1}$, apramycin $50 \text{ mg}\cdot\text{mL}^{-1}$, and arabinose 100 mM.

541
542 All YFP-fusion mutants were generated following the REDIRECT protocol (Supplemental
543 Figure 1) (Gust et al., 2002), by inserting the *eyfp:apramycin* DNA fragment to the C-terminus
544 of individual carboxysome genes based on homologous recombination (Supplemental Table
545 6). Primers used in this work were listed in Supplemental Table 7. The same strategy was
546 also applied for the mYPet mutant. For these mutant strains, BG-11 medium was
547 supplemented with apramycin at $50 \mu\text{g}\cdot\text{mL}^{-1}$.
548

549 **Cell doubling time and growth curve measurement**

550 Cultures were inoculated at OD_{750} of 0.05-0.1 with fresh BG-11. Growth of cells was
551 monitored at OD_{750} using a spectrophotometer (Jenway 6300 spectrophotometer, Jenway,
552 UK) every 24 hours. Doubling times were calculated using exponential phase of growth from
553 day 1 to day 4. Four biological replicates from different culture flasks were recorded. Data are
554 presented as mean \pm standard deviation (SD). For each experiment, at least three biological
555 replicates from different culture flasks were analyzed.
556

557 **Slimfield microscopy and data analysis**

558 Live cells were applied at the small volume onto the BG-11 agarose pad at 0.25 mm
559 thickness to maintain physiological growth, air dried to remove excessive medium and then
560 assembled with plasma cleaned (Harrick-Plasma) glass cover slips. A dual-color bespoke
561 laser excitation single-molecule fluorescence microscope was used utilizing narrow
562 epifluorescence excitation of 10 μm full width at half maximum (FWHM) in the sample plane

563 to generate Slimfield illumination using narrowfield epifluorescence (Wollman and Leake,
564 2016; Wollman et al., 2016b; Wollman et al., 2017). This was incident on a sample mounted
565 on a Mad City Labs nanostage built on an inverted Zeiss microscope body consisting of a 20
566 mW 514 nm wavelength laser. A Chroma GFP/mCherry dichroic was mounted under the
567 Olympus 100x NA = 1.49 TIRF (total internal reflection fluorescence) objective, which delivers
568 10 mW excitation power. The image was split into YFP and chlorophyll channels using a
569 bespoke color splitter utilizing a Chroma dichroic split at 560 nm with 542 nm and 600 nm, 25
570 nm bandwidth filters. Imaging was done with an Andor iXon 128 x 128 pixel EMCCD camera
571 (iXon DV860-BI, Andor Technology, UK), at a pixel magnification of 80 nm/pixel using 5 ms
572 camera exposure time. Excitation intensity was initially reduced by 100x using and ND = 2 or
573 1 attenuation filter for high copy number strains (all except CcmL and RbcX) to avoid pixel
574 saturation on the EMCCD camera detector before a full-power photobleaching. Sample sizes
575 for individual strains are 60 (RbcS), 219 (CcmK3), 77 (CcmK4), 316 (CcmL), 71 (CcmM), 86
576 (CcmN), 95 (CcaA) and 211 (RbcX), respectively. Each population of carboxysomes comes
577 from 20-30 fields of view, with 1-7 cells per field of view.

578

579 The analysis was performed using bespoke MATLAB (Mathworks) software (Miller et al.,
580 2015) with previously outlined methods (Llorente-Garcia et al., 2014; Wollman et al., 2016a;
581 Beattie et al., 2017; Lund et al., 2018; Stracy et al., 2018). In brief, candidate bright
582 fluorescent foci were identified in images using morphological transformation and thresholding.
583 The sub-pixel centroids of these foci were determined using iterative Gaussian masking and
584 their intensity quantified as the summed intensity inside a 5-pixel radius region of interest
585 (ROI) corrected for the mean background intensity inside a surrounding 17 x 17 pixel ROI
586 (Delalez et al., 2010; Leake, 2014). Foci were accepted and tracked through time if they had
587 a signal-to-noise ratio, defined as the mean intensity in the circular ROI divided by the
588 standard deviation in the outer ROI, over 0.4. The characteristic intensity of single
589 YFP/mYPet was measured from the distribution of detected foci intensity towards the end of
590 the photobleaching (Figure 1), confirmed by comparing the obtained value to individual
591 photobleaching steps obtained using edge-preserving filtration (Figure 1) (Leake et al., 2003;
592 Leake et al., 2004). The stoichiometry of foci was then determined through cell-by-cell based
593 Slimfield imaging using numerical integration of pixel intensities (Wollman and Leake, 2015)
594 in each carboxysome divided by the intensity of a single YFP (Figure 1B).

595

596 For high-copy-number strains, intensity of carboxysomes was very high compared to the
597 chlorophyll but for CcmL (typically ~2x, compare Supplemental Figure 3 with Supplemental
598 Figure 4A) the fluorescence intensity per carboxysome was comparable (although generally
599 brighter) to small regions of bright chlorophyll, detected as foci by our software, as confirmed
600 by looking at the parental strain with no YFP present. To correct for this chlorophyll content,
601 we tracked parental WT Syn7942 cells as YFP-labelled cells to calculate the apparent
602 chlorophyll stoichiometry distribution (Supplemental Figure 4A). The CcmL distribution was
603 then corrected by subtracting the apparent chlorophyll distribution. To investigate putative
604 periodic features in the stoichiometry distribution, we used the raw uncorrected values to
605 minimize dephasing artefacts (Figure 4C) using a kernel width of 0.5 molecules (equivalent to
606 the error in determining the characteristic intensity). The peak values in other strains were far
607 from the chlorophyll peak and so unaffected by this correction.

608

609 **Confocal microscopy imaging and data analysis**

610 Preparation of Syn7942 cells for confocal microscopy was performed as described earlier (Liu
611 et al., 2012; Casella et al., 2017). Cells were maintained under different growth conditions
612 prior to microscopy imaging, to ensure full acclimation. Confocal fluorescence images (12-bit,
613 512 x 512 pixels) were recorded using a Zeiss LSM780 with an alpha Plan-Fluor 100x oil
614 immersion objective (NA 1.45) and excitation at 514 nm from an Argon laser. YFP and
615 chlorophyll fluorescence were captured at 520–550 nm and 660–700 nm, respectively. The
616 image pixel size was 41.5 nm. The pixel dwell time was 0.64 μ s and the frame averaging was
617 8, resulting in an effective frame time of ~1.5 s. The pinhole was set to give z axis resolution
618 of 1 μ m. Live-cell confocal fluorescence images were recorded from at least five different
619 cultures. The sample stage was pre-incubated and thermo-controlled at 30°C before and
620 during imaging. Zoom settings were set to have each carboxysome visualized with a
621 minimum of 8 x 8 pixels array to allow sufficient profiling of carboxysome signals by peak
622 intensity recognition and measurement. All images were captured with all pixels below
623 saturation.

624

625 Confocal microscopic images were processed using FIJI Trackmate plugins (Tinevez et al.,
626 2017) to retrieve peak intensities of carboxysomes based on the Find Maxima detection
627 algorithm. Noise tolerance was determined by background intensities in empty regions.
628 Imaging for different treatments in the same strain was performed under the same imaging

629 settings. For strains with visible cytosolic signals, the cytosolic background intensity was
630 determined by the average peak intensities in non-carboxysome regions over the central line
631 of the cell and was subtracted to obtain peak intensities. Raw data were processed by Origin
632 Lab and MATLAB (Mathworks) for profile extraction and statistical analysis and the goodness-
633 of-fit parameter for Violin plot visualization. Violin plots were generated by R to illustrate the
634 fluorescence intensity distribution of individual building proteins per carboxysome fitted by
635 kernel smooth fitting. The representative values and deviations of signal intensities were
636 represented by Peak value \pm half width at half maximum (HWHM) measured from kernel
637 density fitted profiles, respectively. The significance of differences between treatments was
638 evaluated by Mann-Whitney U-tests pair-wisely (Supplemental Table 4). Standard errors of
639 sampling were determined through randomized grouping of intensity entries, with each group
640 containing a minimum of 70–100 entries. Errors were controlled below 5% to have accurate
641 estimation from the distributions. The relative protein abundance of carboxysomes was
642 estimated by confocal imaging under Air/ML, CO₂/ML, LL, and HL was normalized by the
643 definite copy number of each strain under Air/ML determined by Slimfield imaging.

644

645 **Live-cell time-lapse confocal imaging and data analysis**

646 A 2 mm-thick BG-11 agar mat was prepared in stacked sandwiches to accommodate drops of
647 diluted Syn7942 cells. Cells were incubated on the BG-11 agar mat on the microscope for 1-2
648 hours before imaging. The continuous light illumination was provided at the intensity relatively
649 equal to HL, ML, or LL that were used for cell growth, in order to maintain cell physiology. The
650 same illumination was applied to the cells during time-lapse imaging with a hand-made
651 module that switched off the light during laser scanning (less than 5 s per minute intervals).
652 The interval time was set to 60 s to guarantee sufficient light illumination between imaging.
653 The laser power was set to the minimum (1%) to reduce the bleaching for signals during long-
654 term tracking. Images were initially corrected for horizontal drifting by Descriptor-based series
655 registration (2d/3d+T) plugin, and then were processed by the Trackmate plugin in FIJI for
656 particle tracking. Retrieved track data was analyzed using bespoke MATLAB (Mathworks)
657 scripts for MSD. Diffusion coefficient calculations and data visualization were modified as
658 previously described (Ewers et al., 2005; Sbalzarini and Koumoutsakos, 2005). Diffusion
659 coefficients were calculated by fitting the first 6 points of the MSD vs. τ curves. As the MSD
660 vs. τ curves indicated potentially non-Brownian diffusion at higher τ values, we described the
661 diffusion coefficients as “apparent diffusion coefficients”. Tracking and diffusion coefficient

determination were tested by computational simulations (Supplemental Movie 2). Bespoke Matlab code was written to generate simulated image stacks of carboxysomes diffusing inside cells. Images were simulated by integrating a model 3D point spread function over a 3D model for the cell structure (Wollman and Leake 2015). This model comprises an inner cytosol surrounded by thylakoid membranes (indicated by chlorophyll fluorescence) and 3 carboxysomes with a diameter of 200 nm. Each component's intensity was adjusted to match real images before representative Poisson noise was applied. Carboxysomes were simulated undergoing Brownian motion with a diffusion coefficient of $1.3 \times 10^{-5} \mu\text{m}^2 \cdot \text{s}^{-1}$ over 40 image frames. Trackmate tracking and diffusion coefficient calculation yielded a mean diffusion coefficient of $1.32 \pm 0.02 \times 10^{-5} \mu\text{m}^2 \cdot \text{s}^{-1}$, giving a 1.5% error.

672

673 **Immunoblot analysis**

Immunoblot examination was carried out following the procedure described previously (Sun et al., 2016). 150 μg of cell lysate, measured by Pierce Coomassie (Bradford) Protein Assay Kit (Thermo Fisher Scientific), was loaded on 10% (v/v) denaturing SDS-PAGE gels. Immunoblot analysis was performed using the primary mouse monoclonal anti-GFP (Invitrogen, 33-2600), capable of recognizing series of GFP variants including YFP, the rabbit polyclonal anti-RbcL (Agrisera, AS03 037), the horseradish peroxidase-conjugated goat anti-mouse IgG secondary antibody (Promega, W4021) and a Goat anti-Rabbit IgG (H&L), HRP conjugated (Agrisera AS10 1461). Anti-CcmK2 antibody was kindly provided by the Kerfeld lab (Michigan State University, US) (Cai et al., 2016). Protein quantification from immunoblot data was carried out using FIJI. Our nominal assumption that the ratios of YFP-tagged to total RbcL or CcmK2 in carboxysomes are similar to those in cell lysates.

685

686 ***In vivo* carbon fixation assay**

In vivo carbon fixation assay was carried out to determine carbon fixation of Syn7942 WT and mutant cells, as described in the previous work (Sun et al., 2016). For each WT and mutant, at least three biological replicates from different culture flasks were assayed. Significance was assessed by two-tailed Student's t-tests.

691

692 **Electron microscopy and carboxysome size measurement**

693 Electron microscopy was carried out as described previously (Liu et al., 2008; Sun et al.,
694 2016). Carboxysome diameter was measured as described previously (Faulkner et al., 2017)
695 and was analyzed using Origin.

696

697 **Accession Numbers**

698 Accession numbers of genes in this article are provided in Supplemental Table 6.

699

700 **Supplemental Data**

701 **Supplemental Figure 1.** Construction and verification of Syn7942 strains with YFP fusion to
702 individual carboxysome proteins.

703 **Supplemental Figure 2.** Immunoblot analysis of the YFP-tagged Syn7942 strains using the
704 anti-GFP, anti-RbcL and anti-CcmK antibodies of soluble fractions in this study based on
705 SDS-PAGE.

706 **Supplemental Figure 3.** Slimfield images of YFP-fusion cells under Air/ML and stoichiometric
707 histogram of copies of YFP molecules per carboxysome.

708 **Supplemental Figure 4.** Normalization of chlorophyll during Slimfield imaging for Syn7942
709 strains.

710 **Supplemental Figure 5.** Comparison of YFP and mYPet tagging to RbcL reveals no
711 differences in carboxysome localization, cell growth and carbon fixation, suggesting that there
712 are no measurable artefacts due to putative effects of dimerization of the YFP tag.

713 **Supplemental Figure 6.** Confocal images of YFP-tagged cells.

714 **Supplemental Figure 7.** Confocal images of RbcS-YFP, CcmM-YFP, CcmK4-YFP and
715 CcmK3-YFP cells under Air/ML, CO₂, LL, and HL and distribution profiles of carboxysome
716 protein signal intensity.

717 **Supplemental Figure 8.** Confocal images of CcmL-YFP, CcmN-YFP, CcaA-YFP and RbcX-
718 YFP cells under Air/ML, CO₂, LL, and HL and distribution profiles of carboxysome protein
719 signal intensity (continuing Supplemental Figure 7).

720 **Supplemental Figure 9.** Thin-section EM images of WT Syn7942 cells under Air/ML, CO₂/ML,
721 LL and HL.

722 **Supplemental Figure 10.** Changes in the diffusion coefficient of carboxysomes in Syn7942
723 cells under HL, ML and LL are not dependent on the carboxysome size.

724 **Supplemental Figure 11.** CcmP-YFP and CcmO-YFP Syn7942 cells.

725 **Supplemental Table 1.** Cell growth, carbon fixation and cell dimensions of Syn7942 WT and
726 YFP-fusion mutants under Air/ML.
727 **Supplemental Table 2.** Immunoblotting estimation of the stoichiometry of carboxysomal
728 proteins in cell lysates.
729 **Supplemental Table 3.** Carboxysome content per cell under Air/ML, CO₂/ML, LL and HL
730 determined by confocal imaging.
731 **Supplemental Table 4.** Evaluation and quality control of quantitative microscopy.
732 **Supplemental Table 5.** Carboxysome properties in Syn7942 vary under Air/ML, CO₂/ML, LL
733 and HL, determined by Slimfield, confocal and EM imaging.
734 **Supplemental Table 6.** Accession numbers for genes/proteins in this work.
735 **Supplemental Table 7.** PCR primers used in this study for gene cloning and sequencing.
736 **Supplemental Movie 1.** Time-lapse confocal imaging reveals different diffusion dynamics of
737 carboxysomes in the RbcL-YFP Syn7942 cells grown under HL, ML and LL conditions.
738 **Supplemental Movie 2.** Simulations of diffusing carboxysomes *in cellulo* validate tracking
739 and diffusion coefficient determination.

740

741 **Acknowledgements**

742 We thank Gregory F Dykes, Selene Casella and Alison Beckett for technical support of
743 electron microscopy. We thank David Mason in confocal image analysis. We thank the
744 Liverpool Centre for Cell Imaging for technical assistance and provision. Y.S., F.H. and L.-N.L.
745 were supported by Royal Society (UF120411, IE131399, RGF\EA\180233, RGF\EA\181061
746 and URF\R\180030, L.-N.L.) and Biotechnology and Biological Sciences Research Council
747 Grant (BB/M024202/1 and BB/R003890/1, L.-N.L.), Leverhulme Trust (ECF-2016-778, F.H.)
748 and China Scholarship Council (Y.S.). M.L. was supported by a Medical Research Council
749 grant (MR/K01580X/1), Biotechnology and Biological Sciences Research Council Grant
750 (BB/N006453/1). A.J.M.W. was part-funded by the Wellcome Trust (204829) through Centre
751 for Future Health at the University of York.

752

753

754 **Author contributions**

755 L.-N.L. and M.C.L. designed research; Y.Q. A.J.M.W. and F.H. performed research and
756 analyzed data; L.-N.L., Y.Q., M.C.L., and A.J.M.W. wrote the paper.

757

758

759 **Competing interests**

760 The authors declare no conflict of interest.

761

762

763 **Figure legends**

764 **Figure 1. Slimfield quantification of cells grown under ambient air/moderate light** 765 **Air/ML conditions.**

766 **(A)** Averaged Slimfield images of YFP fluorescence (green) over 5 frames of strains
767 expressing shell component CcmK4-YFP, the interior enzyme RbcS-YFP, and the shell-
768 interior linker protein CcmM-YFP. White dashed lines indicate cell body outlines.

769 **(B)** Distribution of the intensities of automatically detected foci from the end of
770 photobleaching, corresponding to the characteristic intensity of *in vivo* YFP. Inset shows the
771 Fourier spectrum of ‘overtracked’ foci, tracked beyond photobleaching, showing a peak at the
772 characteristic intensity.

773 **(C)** Representative fluorescence photobleaching tracked at ultra-fast speed. The CcmK4 plot
774 shows an inset ‘zoomed in’ on lower intensity range with step-preserving Chung-Kennedy
775 filtered data in red, showing individual photobleaching steps clearly visible at the
776 characteristic intensity. Brightness (kcounts), counts measured per camera pixel multiplied by
777 1,000.

778 **(D)** Distribution of YFP copy number detected for individual carboxysomes in corresponding
779 mutants, rendered as kernel density estimates using standard kernel width. Heterogeneity of
780 contents was observed, and a “preferable” copy number, represented by kernel density peak
781 values could be determined. Statistics of copy numbers (Peak value \pm HWHM) are listed in
782 Table 1 for ML conditions. The corresponding Slimfield images and histogram for complete
783 strain sets are shown in Supplemental Figure 3.

784

785 **Figure 2. Relative protein quantification of CcmK4, RbcS and CcmM in the** 786 **carboxysome under different CO₂ levels and light intensities using confocal** 787 **microscopy.**

788 **(A)** Confocal images of CcmK4-YFP, RbcS-YFP and CcmM-YFP strains under Air/ML,
789 CO₂/ML, LL and HL. Fluorescence foci (green) indicate carboxysomes, and cell borders were
790 outlined by white dashed lines. Scale bar indicates 2 μ m.

791 **(B)** Violin plot of carboxysome intensities under Air/ML, CO₂/ML, LL and HL, normalized to
792 kernel density ML peak values (peaks marked by white dashed lines).

793 **(C)** Kernel density estimates of CcmL carboxysome copy number grown under Air/ML, CO₂,
794 LL and HL detected by Slimfield and corrected for chlorophyll. Triple Gaussian fits are
795 indicated as colored dashed lines with the summed fit in red. The percentage in each
796 Gaussian is indicated aside.

797

798 **Figure 3. Changes in carboxysome protein stoichiometry upon increases in CO₂ levels** 799 **and light intensity.**

800 **(A)** Comparison of carboxysome protein stoichiometry under CO₂ treatment. Increase in the
801 CO₂ concentration resulted in the rise of CcmK3, CcmK4, CcaA and CcmL contents and the
802 decline of RbcS, CcmN and CcmM contents.

803 **(B)** Comparison of carboxysome protein stoichiometry under light intensity treatment.
 804 Increased light intensity led to the elevation of RbcS, CcmM, CcmL, CcaA and CcmN
 805 contents, whereas the abundance of RbcX, CcmK3 and CcmK4 contents per carboxysome
 806 did not change dramatically.
 807 Mann-Whitney U-tests were performed to compare the numbers of functional units of
 808 individual carboxysome proteins changed from CO₂/ML to Air/ML (A) and from HL to LL (B). *,
 809 $p < 0.05$; ***, $p < 0.005$; ns, $p > 0.05$.
 810

811 **Figure 4. Variations of the carboxysome size and carbon fixation under Air/ML, CO₂, LL**
 812 **and HL.**

813 **(A)** Thin-section electron microscopy (EM) images showing individual carboxysomes in the
 814 Syn7942 WT cells under Air/ML, CO₂, LL and HL treatments Yellow arrows indicate the
 815 carboxysomes with spaces of low protein density under LL. More EM images are shown in
 816 Supplemental Figure 9. Scale bar indicates 1 μ m.

817 **(B)** Changes in the carboxysome diameter under Air/ML, CO₂, LL and HL measured from EM
 818 ($n = 33, 25, 27$ and 51 , respectively), with representative carboxysome images depicted
 819 above. Dashed lines indicate medians and solid lines indicate means. Differences in the
 820 carboxysome diameter are significant between CO₂ and air ($p = 1.92 \times 10^{-14}$) and between LL
 821 and HL ($p = 8.29 \times 10^{-7}$), indicated as ***.

822 **(C)** Correlation between the carboxysome size and the Rubisco content per carboxysome
 823 under Air/ML, CO₂, LL and HL.

824 **(D)** Correlation between the carboxysome size and CO₂ fixation per carboxysome.

825 **(E)** Correlation between the carboxysome size and CO₂ fixation per Rubisco of the
 826 carboxysomes. Carboxysome diameters and CO₂ fixation are presented as average \pm SD,
 827 whereas the carboxysome total protein content and Rubisco content are shown as Peak
 828 value \pm HWHM.
 829

830 **Figure 5. Spatial localization and diffusion dynamics of carboxysomes in Syn7942 cells**
 831 **are dependent on light intensity.**

832 **(A)** Tracking of carboxysome diffusion in cells grown under HL, ML and LL. Colored lines
 833 indicate the diffusion trajectories of each carboxysomes and circles represent the diffusion
 834 areas of each carboxysomes over 60 mins. Scale bar indicates 1 μ m.

835 **(B)** Non-linear MSD (Mean Square Displacement) vs. the time interval (τ) profiles suggest the
 836 mobility of carboxysomes in Syn7942 cells grown under HL, ML and LL. Inset, zoom-in view
 837 of the MSD profile under LL.

838 **(C)** Diffusion coefficient of carboxysomes *in vivo* decreases significantly when the light
 839 intensity reduces: $2.76 \pm 2.83 \times 10^{-5} \mu\text{m}^2 \cdot \text{s}^{-1}$ for HL (mean \pm SD, $n = 105$), $1.48 \pm 1.03 \times 10^{-5}$
 840 $\mu\text{m}^2 \cdot \text{s}^{-1}$ for ML ($n = 84$), and $0.28 \pm 0.19 \times 10^{-5} \mu\text{m}^2 \cdot \text{s}^{-1}$ for LL ($n = 336$). $p = 3.05 \times 10^{-5}$
 841 between HL and ML; $p = 2.77 \times 10^{-5}$ between ML and LL, two-tailed Student's t-test).
 842

843 **Figure 6. Model of the β -carboxysome structure and protein stoichiometry.**

844 **(A)** Diagram of an icosahedral carboxysome structure and organization of building
 845 components. The stoichiometry of each building component within the carboxysome and its
 846 variations in response to changes in CO₂ and light intensity are shown on the right (See also
 847 Table 1). *Rubisco content was estimated from RbcS stoichiometry based on the RbcL₈S₈
 848 Rubisco structure. The majority of shell facets shown in light blue is tiled by the major shell

849 protein CcmK2. The total abundance of CcmM58 and CcmM35 was estimated. The
850 components RbcL, CcmK2, CcmO and CcmP were not directly determined in this work and
851 thus are not shown in this model.
852 **(B)** The carboxysome diameter is variable in response to changes in the CO₂ level and light
853 intensity.
854

Table 1. Protein stoichiometry of the Syn7942 β -carboxysome and its variability in cells grown under Air/ML, CO₂/ML, LL and HL conditions determined from Slimfield and confocal microscopy. Stoichiometry is presented as Peak value \pm HWHM and the sample sizes are indicated as *n*. Peak values were determined from Slimfield stoichiometry profiles of each carboxysome proteins (Figure 1, Supplemental Figure 3). Quantification of CcmL under the four conditions was acquired from Slimfield for accurate measurement of copies of shell pentamers for capping the carboxysome structure. Copies of other carboxysome proteins were calculated using Slimfield results (bold) with definitive counts of protein copies under Air/ML (See also Supplemental Figure 3) in combination with relative quantification of each protein under the four conditions from confocal imaging (See also Supplemental Figure 7 and 8). Protein structures were derived from previous studies (Kerfeld et al., 2005; Long et al., 2007; Tanaka et al., 2007; Tanaka et al., 2008; Long et al., 2011; Kinney et al., 2012; McGurn et al., 2016). *Monomeric unit of CcmM was designated to CcmM35 that is the majority of CcmM; CcmM58 is postulated as a trimer.

Category	Structure	Protein	Air/ML		CO ₂ /ML		LL		HL	
			Peak value \pm HWHM	Number of functional units	Peak value \pm HWHM	Number of functional units	Peak value \pm HWHM	Number of functional units	Peak value \pm HWHM	Number of functional units
Shell proteins	Hexamer	CcmK3	92 \pm 148 (<i>n</i> = 219)	15 \pm 25	172 \pm 83 (<i>n</i> = 2048)	29 \pm 14	83 \pm 31 (<i>n</i> = 1516)	14 \pm 5	87 \pm 52 (<i>n</i> = 2155)	14 \pm 9
		CcmK4	314 \pm 194 (<i>n</i> = 77)	52 \pm 32	562 \pm 263 (<i>n</i> = 1918)	94 \pm 44	313 \pm 121 (<i>n</i> = 1766)	52 \pm 20	304 \pm 95 (<i>n</i> = 3215)	51 \pm 16
	Pentamer	CcmL	37 \pm 17 (<i>n</i> = 316)	7.4 \pm 3.4	66 \pm 24 (<i>n</i> = 311)	13.2 \pm 4.8	34 \pm 15 (<i>n</i> = 394)	6.8 \pm 3.0	69 \pm 24 (<i>n</i> = 220)	13.8 \pm 4.8
Structural proteins	Monomer*	CcmM	719 \pm 1433 (<i>n</i> = 71)	719 \pm 1433	468 \pm 425 (<i>n</i> = 2313)	468 \pm 425	483 \pm 366 (<i>n</i> = 3655)	483 \pm 366	1176 \pm 691 (<i>n</i> = 2318)	1176 \pm 691
	Monomer	CcmN	74 \pm 51 (<i>n</i> = 86)	74 \pm 51	52 \pm 28 (<i>n</i> = 3143)	52 \pm 28	51 \pm 20 (<i>n</i> = 4022)	51 \pm 20	82 \pm 34 (<i>n</i> = 5074)	82 \pm 34
CA	Hexamer	CcaA	86 \pm 81 (<i>n</i> = 95)	14 \pm 14	129 \pm 86 (<i>n</i> = 1354)	21 \pm 14	65 \pm 21 (<i>n</i> = 217)	11 \pm 4	122 \pm 59 (<i>n</i> = 2837)	20 \pm 10
Rubisco enzyme	L ₈ S ₈	RbcS	6822 \pm 9200 (<i>n</i> = 60)	853 \pm 1150	4401 \pm 6655 (<i>n</i> = 894)	550 \pm 832	2934 \pm 5492 (<i>n</i> = 752)	367 \pm 687	12057 \pm 5186 (<i>n</i> = 1974)	1507 \pm 648
Rubisco chaperone	Dimer	RbcX	39 \pm 32 (<i>n</i> = 211)	20 \pm 16	38 \pm 10 (<i>n</i> = 1370)	19 \pm 5	40 \pm 9 (<i>n</i> = 1402)	20 \pm 5	40 \pm 9 (<i>n</i> = 1861)	20 \pm 5

866

867

Parsed Citations

Axen, S.D., Erbilgin, O., and Kerfeld, C.A. (2014). A taxonomy of bacterial microcompartment loci constructed by a novel scoring method. *PLoS Comput Biol* 10, e1003898.

Pubmed: [Author and Title](#)

Google Scholar: [Author Only](#) [Title Only](#) [Author and Title](#)

Badrinarayanan, A., Reyes-Lamothe, R., Uphoff, S., Leake, M.C., and Sherratt, D.J. (2012). In vivo architecture and action of bacterial structural maintenance of chromosome proteins. *Science* 338, 528-531.

Pubmed: [Author and Title](#)

Google Scholar: [Author Only](#) [Title Only](#) [Author and Title](#)

Beattie, T.R., Kapadia, N., Nicolas, E., Uphoff, S., Wollman, A.J., Leake, M.C., and Reyes-Lamothe, R. (2017). Frequent exchange of the DNA polymerase during bacterial chromosome replication. *eLife* 6, e21763.

Pubmed: [Author and Title](#)

Google Scholar: [Author Only](#) [Title Only](#) [Author and Title](#)

Bobik, T.A., Lehman, B.P., and Yeates, T.O. (2015). Bacterial microcompartments: widespread prokaryotic organelles for isolation and optimization of metabolic pathways. *Mol Microbiol* 98, 193-207.

Pubmed: [Author and Title](#)

Google Scholar: [Author Only](#) [Title Only](#) [Author and Title](#)

Cai, F., Menon, B.B., Cannon, G.C., Curry, K.J., Shively, J.M., and Heinhorst, S. (2009). The pentameric vertex proteins are necessary for the icosahedral carboxysome shell to function as a CO₂ leakage barrier. *PLoS One* 4, e7521.

Pubmed: [Author and Title](#)

Google Scholar: [Author Only](#) [Title Only](#) [Author and Title](#)

Cai, F., Sutter, M., Cameron, J.C., Stanley, D.N., Kinney, J.N., and Kerfeld, C.A. (2013). The structure of CcmP, a tandem bacterial microcompartment domain protein from the beta-carboxysome, forms a subcompartment within a microcompartment. *J Biol Chem* 288, 16055-16063.

Pubmed: [Author and Title](#)

Google Scholar: [Author Only](#) [Title Only](#) [Author and Title](#)

Cai, F., Bernstein, S.L., Wilson, S.C., and Kerfeld, C.A. (2016). Production and characterization of synthetic carboxysome shells with incorporated luminal proteins. *Plant Physiol* 170, 1868-1877.

Pubmed: [Author and Title](#)

Google Scholar: [Author Only](#) [Title Only](#) [Author and Title](#)

Cameron, J.C., Wilson, S.C., Bernstein, S.L., and Kerfeld, C.A. (2013). Biogenesis of a bacterial organelle: the carboxysome assembly pathway. *Cell* 155, 1131-1140.

Pubmed: [Author and Title](#)

Google Scholar: [Author Only](#) [Title Only](#) [Author and Title](#)

Casella, S., Huang, F., Mason, D., ZHAO, G.Y., Johnson, G.N., Mullineaux, C.W., and Liu, L.N. (2017). Dissecting the native architecture and dynamics of cyanobacterial photosynthetic machinery. *Mol Plant* 10, 1434-1448.

Pubmed: [Author and Title](#)

Google Scholar: [Author Only](#) [Title Only](#) [Author and Title](#)

Chen, A.H., Robinson-Mosher, A., Savage, D.F., Silver, P.A., and Polka, J.K. (2013). The bacterial carbon-fixing organelle is formed by shell envelopment of preassembled cargo. *PloS One* 8, e76127.

Pubmed: [Author and Title](#)

Google Scholar: [Author Only](#) [Title Only](#) [Author and Title](#)

Dai, W., Chen, M., Myers, C., Ludtke, S.J., Montgomery Pettitt, B., King, J.A., Schmid, M.F., and Chiu, W. (2018). Visualizing individual RuBisCO and its assembly into carboxysomes in marine cyanobacteria by cryo-electron tomography. *J Mol Biol*.

Pubmed: [Author and Title](#)

Google Scholar: [Author Only](#) [Title Only](#) [Author and Title](#)

Delalez, N.J., Wadhams, G.H., Rosser, G., Xue, Q., Brown, M.T., Dobbie, I.M., Berry, R.M., Leake, M.C., and Armitage, J.P. (2010). Signal-dependent turnover of the bacterial flagellar switch protein FliM. *Proc Natl Acad Sci U S A* 107, 11347-11351.

Pubmed: [Author and Title](#)

Google Scholar: [Author Only](#) [Title Only](#) [Author and Title](#)

Dou, Z., Heinhorst, S., Williams, E.B., Murin, C.D., Shively, J.M., and Cannon, G.C. (2008). CO₂ fixation kinetics of *Halothiobacillus neapolitanus* mutant carboxysomes lacking carbonic anhydrase suggest the shell acts as a diffusional barrier for CO₂. *J Biol Chem* 283, 10377-10384.

Pubmed: [Author and Title](#)

Google Scholar: [Author Only](#) [Title Only](#) [Author and Title](#)

Emlyn-Jones, D., Woodger, F.J., Price, G.D., and Whitney, S.M. (2006). RbcX can function as a rubisco chaperonin, but is non-essential in *Synechococcus* PCC7942. *Plant Cell Physiol* 47, 1630-1640.

Pubmed: [Author and Title](#)

Google Scholar: [Author Only](#) [Title Only](#) [Author and Title](#)

Ewers, H., Smith, A.E., Sbalzarini, I.F., Lilie, H., Koumoutsakos, P., and Helenius, A (2005). Single-particle tracking of murine polyoma virus-like particles on live cells and artificial membranes. *Proc Natl Acad Sci U S A* 102, 15110-15115.

Pubmed: [Author and Title](#)

Google Scholar: [Author Only](#) [Title Only](#) [Author and Title](#)

Fang, Y., Huang, F., Faulkner, M., Jiang, Q., Dykes, G.F., Yang, M., and Liu, L.N. (2018). Engineering and modulating functional cyanobacterial CO₂-fixing organelles. *Frontiers Plant Sci* 9, 739.

Pubmed: [Author and Title](#)

Google Scholar: [Author Only](#) [Title Only](#) [Author and Title](#)

Faulkner, M., Zhao, L.S., Barrett, S., and Liu, L.N. (2019). Self-assembly stability and variability of bacterial microcompartment shell proteins in response to the environmental change. *Nanoscale Research Letters* 14, 54.

Pubmed: [Author and Title](#)

Google Scholar: [Author Only](#) [Title Only](#) [Author and Title](#)

Faulkner, M., Rodriguez-Ramos, J., Dykes, G.F., Owen, S.V., Casella, S., Simpson, D.M., Beynon, R.J., and Liu, L.-N. (2017). Direct characterization of the native structure and mechanics of cyanobacterial carboxysomes. *Nanoscale* 9, 10662–10673.

Pubmed: [Author and Title](#)

Google Scholar: [Author Only](#) [Title Only](#) [Author and Title](#)

Gust, B., Kieser, T., and Chater, K.F. (2002). REDIRECT Technology: PCR-targeting System in *Streptomyces coelicolor*. (Norwich: John Innes Centre).

Pubmed: [Author and Title](#)

Google Scholar: [Author Only](#) [Title Only](#) [Author and Title](#)

Hagen, A., Sutter, M., Sloan, N., and Kerfeld, C.A (2018a). Programmed loading and rapid purification of engineered bacterial microcompartment shells. *Nature Commun* 9, 2881.

Pubmed: [Author and Title](#)

Google Scholar: [Author Only](#) [Title Only](#) [Author and Title](#)

Hagen, A.R., Plegaria, J.S., Sloan, N., Ferlez, B., Aussignargues, C., Burton, R., and Kerfeld, C.A (2018b). In vitro assembly of diverse bacterial microcompartment shell architectures. *Nano Lett* 18, 7030-7037.

Pubmed: [Author and Title](#)

Google Scholar: [Author Only](#) [Title Only](#) [Author and Title](#)

Harano, K., Ishida, H., Kittaka, R., Kojima, K., Inoue, N., Tsukamoto, M., Satoh, R., Himeno, M., Iwaki, T., and Wadano, A (2003). Regulation of the expression of ribulose-1,5-bisphosphate carboxylase/oxygenase (EC 4.1.1.39) in a cyanobacterium, *Synechococcus* PCC7942. *Photosynth Res* 78, 59-65.

Pubmed: [Author and Title](#)

Google Scholar: [Author Only](#) [Title Only](#) [Author and Title](#)

Huang, F., Vasieva, O., Sun, Y., Faulkner, M., Dykes, G.F., Zhao, Z., and Liu, L.N. (2019). Roles of RbcX in carboxysome biosynthesis in the cyanobacterium *Synechococcus elongatus* PCC7942. *Plant Physiol* 179, 184-194.

Pubmed: [Author and Title](#)

Google Scholar: [Author Only](#) [Title Only](#) [Author and Title](#)

Iancu, C.V., Morris, D.M., Dou, Z., Heinhorst, S., Cannon, G.C., and Jensen, G.J. (2010). Organization, structure, and assembly of alpha-carboxysomes determined by electron cryotomography of intact cells. *J Mol Biol* 396, 105-117.

Pubmed: [Author and Title](#)

Google Scholar: [Author Only](#) [Title Only](#) [Author and Title](#)

Iancu, C.V., Ding, H.J., Morris, D.M., Dias, D.P., Gonzales, A.D., Martino, A., and Jensen, G.J. (2007). The structure of isolated *Synechococcus* strain WH8102 carboxysomes as revealed by electron cryotomography. *J Mol Biol* 372, 764-773.

Pubmed: [Author and Title](#)

Google Scholar: [Author Only](#) [Title Only](#) [Author and Title](#)

Jain, I.H., Vijayan, V., and O'Shea, E.K. (2012). Spatial ordering of chromosomes enhances the fidelity of chromosome partitioning in cyanobacteria. *Proc Natl Acad Sci U S A* 109, 13638-13643.

Pubmed: [Author and Title](#)

Google Scholar: [Author Only](#) [Title Only](#) [Author and Title](#)

Kerfeld, C.A., and Erbilgin, O. (2015). Bacterial microcompartments and the modular construction of microbial metabolism. *Trends Microbiol* 23, 22-34.

Pubmed: [Author and Title](#)

Google Scholar: [Author Only](#) [Title Only](#) [Author and Title](#)

Kerfeld, C.A., and Melnicki, M.R. (2016). Assembly, function and evolution of cyanobacterial carboxysomes. *Curr Opin Plant Biol* 31, 66-75.

Pubmed: [Author and Title](#)

Google Scholar: [Author Only](#) [Title Only](#) [Author and Title](#)

Kerfeld, C.A., Aussignargues, C., Zarzycki, J., Cai, F., and Sutter, M. (2018). Bacterial microcompartments. *Nat Rev Microbiol* 16, 277-290.

Pubmed: [Author and Title](#)

Google Scholar: [Author Only](#) [Title Only](#) [Author and Title](#)

Kerfeld, C.A., Sawaya, M.R., Tanaka, S., Nguyen, C.V., Phillips, M., Beeby, M., and Yeates, T.O. (2005). Protein structures forming the shell of primitive bacterial organelles. *Science* 309, 936-938.

Pubmed: [Author and Title](#)

Google Scholar: [Author Only Title Only Author and Title](#)

Kinney, J.N., Salmeen, A., Cai, F., and Kerfeld, C.A. (2012). Elucidating essential role of conserved carboxysomal protein CcmN reveals common feature of bacterial microcompartment assembly. *J Biol Chem* 287, 17729-17736.

Pubmed: [Author and Title](#)

Google Scholar: [Author Only Title Only Author and Title](#)

Larsson, A.M., Hasse, D., Vaeleard, K., and Andersson, I. (2017). Crystal structures of β -carboxysome shell protein CcmP: ligand binding correlates with the closed or open central pore. *J Exp Bot* 68, 3857-3867.

Pubmed: [Author and Title](#)

Google Scholar: [Author Only Title Only Author and Title](#)

Lassila, J.K., Bernstein, S.L., Kinney, J.N., Axen, S.D., and Kerfeld, C.A. (2014). Assembly of robust bacterial microcompartment shells using building blocks from an organelle of unknown function. *J Mol Biol* 426, 2217-2228.

Pubmed: [Author and Title](#)

Google Scholar: [Author Only Title Only Author and Title](#)

Leake, M.C. (2014). Analytical tools for single-molecule fluorescence imaging in cellulose. *Physical Chemistry Chemical Physics* 16, 12635-12647.

Pubmed: [Author and Title](#)

Google Scholar: [Author Only Title Only Author and Title](#)

Leake, M.C. (2018). Transcription factors in eukaryotic cells can functionally regulate gene expression by acting in oligomeric assemblies formed from an intrinsically disordered protein phase transition enabled by molecular crowding. *Transcription* 9, 298-306.

Pubmed: [Author and Title](#)

Google Scholar: [Author Only Title Only Author and Title](#)

Leake, M.C., Wilson, D., Bullard, B., and Simmons, R.M. (2003). The elasticity of single kettin molecules using a two-bead laser-tweezers assay. *FEBS Lett* 535, 55-60.

Pubmed: [Author and Title](#)

Google Scholar: [Author Only Title Only Author and Title](#)

Leake, M.C., Wilson, D., Gautel, M., and Simmons, R.M. (2004). The elasticity of single titin molecules using a two-bead optical tweezers assay. *Biophys J* 87, 1112-1135.

Pubmed: [Author and Title](#)

Google Scholar: [Author Only Title Only Author and Title](#)

Leake, M.C., Chandler, J.H., Wadhams, G.H., Bai, F., Berry, R.M., and Armitage, J.P. (2006). Stoichiometry and turnover in single, functioning membrane protein complexes. *Nature* 443, 355-358.

Pubmed: [Author and Title](#)

Google Scholar: [Author Only Title Only Author and Title](#)

Leake, M.C., Greene, N.P., Godun, R.M., Granjon, T., Buchanan, G., Chen, S., Berry, R.M., Palmer, T., and Berks, B.C. (2008). Variable stoichiometry of the TatA component of the twin-arginine protein transport system observed by in vivo single-molecule imaging. *Proc Natl Acad Sci U S A* 105, 15376-15381.

Pubmed: [Author and Title](#)

Google Scholar: [Author Only Title Only Author and Title](#)

Lenn, T., Leake, M.C., and Mullineaux, C.W. (2008). Clustering and dynamics of cytochrome bd-I complexes in the Escherichia coli plasma membrane in vivo. *Mol Microbiol* 70, 1397-1407.

Pubmed: [Author and Title](#)

Google Scholar: [Author Only Title Only Author and Title](#)

Li, Q., Yafal, A.G., Lee, Y.M., Hogle, J., and Chow, M. (1994). Poliovirus neutralization by antibodies to internal epitopes of VP4 and VP1 results from reversible exposure of these sequences at physiological temperature. *J Virol* 68, 3965-3970.

Pubmed: [Author and Title](#)

Google Scholar: [Author Only Title Only Author and Title](#)

Liberton, M., Austin, J.R., 2nd, Berg, R.H., and Pakrasi, H.B. (2011). Unique thylakoid membrane architecture of a unicellular N₂-fixing cyanobacterium revealed by electron tomography. *Plant Physiol* 155, 1656-1666.

Pubmed: [Author and Title](#)

Google Scholar: [Author Only Title Only Author and Title](#)

Lin, M.T., Occhialini, A., Andralojc, P.J., Parry, M.A.J., and Hanson, M.R. (2014a). A faster Rubisco with potential to increase photosynthesis in crops. *Nature* 513, 547-550.

Pubmed: [Author and Title](#)

Google Scholar: [Author Only Title Only Author and Title](#)

Lin, M.T., Occhialini, A., Andralojc, P.J., Devonshire, J., Hines, K.M., Parry, M.A., and Hanson, M.R. (2014b). β -Carboxysomal proteins assemble into highly organized structures in Nicotiana chloroplasts. *Plant J* 79, 1-12.

Pubmed: [Author and Title](#)
Google Scholar: [Author Only Title Only Author and Title](#)

Liu, L.N., Aartsma, T.J., Thomas, J.C., Lamers, G.E., Zhou, B.C., and Zhang, Y.Z. (2008). Watching the native supramolecular architecture of photosynthetic membrane in red algae: topography of phycobilisomes and their crowding, diverse distribution patterns. J Biol Chem 283, 34946-34953.

Pubmed: [Author and Title](#)
Google Scholar: [Author Only Title Only Author and Title](#)

Liu, L.N., Bryan, S.J., Huang, F., Yu, J.F., Nixon, P.J., Rich, P.R., and Mullineaux, C.W. (2012). Control of electron transport routes through redox-regulated redistribution of respiratory complexes. Proc Natl Acad Sci U S A 109, 11431-11436.

Pubmed: [Author and Title](#)
Google Scholar: [Author Only Title Only Author and Title](#)

Llorente-Garcia, I., Lenn, T., Erhardt, H., Harriman, O.L., Liu, L.N., Robson, A., Chiu, S.W., Matthews, S., Willis, N.J., Bray, C.D., Lee, S.H., Shin, J.Y., Bustamante, C., Liphardt, J., Friedrich, T., Mullineaux, C.W., and Leake, M.C. (2014). Single-molecule in vivo imaging of bacterial respiratory complexes indicates delocalized oxidative phosphorylation. Biochim Biophys Acta 1837, 811-824.

Pubmed: [Author and Title](#)
Google Scholar: [Author Only Title Only Author and Title](#)

Long, B.M., Price, G.D., and Badger, M.R. (2005). Proteomic assessment of an established technique for carboxysome enrichment from *Synechococcus* PCC7942. Can J Bot 83, 746-757.

Pubmed: [Author and Title](#)
Google Scholar: [Author Only Title Only Author and Title](#)

Long, B.M., Badger, M.R., Whitney, S.M., and Price, G.D. (2007). Analysis of carboxysomes from *Synechococcus* PCC7942 reveals multiple Rubisco complexes with carboxysomal proteins CcmM and CcaA. J Biol Chem 282, 29323-29335.

Pubmed: [Author and Title](#)
Google Scholar: [Author Only Title Only Author and Title](#)

Long, B.M., Tucker, L., Badger, M.R., and Price, G.D. (2010). Functional cyanobacterial β -carboxysomes have an absolute requirement for both long and short forms of the CcmM protein. Plant Physiol 153, 285-293.

Pubmed: [Author and Title](#)
Google Scholar: [Author Only Title Only Author and Title](#)

Long, B.M., Rae, B.D., Badger, M.R., and Price, G.D. (2011). Over-expression of the beta-carboxysomal CcmM protein in *Synechococcus* PCC7942 reveals a tight co-regulation of carboxysomal carbonic anhydrase (CcaA) and M58 content. Photosynth Res 109, 33-45.

Pubmed: [Author and Title](#)
Google Scholar: [Author Only Title Only Author and Title](#)

Long, B.M., Hee, W.Y., Sharwood, R.E., Rae, B.D., Kaines, S., Lim, Y.-L., Nguyen, N.D., Massey, B., Bala, S., von Caemmerer, S., Badger, M.R., and Price, G.D. (2018). Carboxysome encapsulation of the CO₂-fixing enzyme Rubisco in tobacco chloroplasts. Nature Commun 9, 3570.

Pubmed: [Author and Title](#)
Google Scholar: [Author Only Title Only Author and Title](#)

Lund, V.A., Wacnik, K., Turner, R.D., Cotterell, B.E., Walther, C.G., Fenn, S.J., Grein, F., Wollman, A.J., Leake, M.C., Olivier, N., Cadby, A., Mesnage, S., Jones, S., and Foster, S.J. (2018). Molecular coordination of *Staphylococcus aureus* cell division. eLife 7, e32057.

Pubmed: [Author and Title](#)
Google Scholar: [Author Only Title Only Author and Title](#)

MacCready, J.S., Hakim, P., Young, E.J., Hu, L., Liu, J., Osteryoung, K.W., Vecchiarelli, A.G., and Ducat, D.C. (2018). Protein gradients on the nucleoid position the carbon-fixing organelles of cyanobacteria. eLife 7, e39723.

Pubmed: [Author and Title](#)
Google Scholar: [Author Only Title Only Author and Title](#)

McGinn, P.J., Price, G.D., Maleszka, R., and Badger, M.R. (2003). Inorganic carbon limitation and light control the expression of transcripts related to the CO₂-concentrating mechanism in the cyanobacterium *Synechocystis* sp. strain PCC6803. Plant Physiol 132, 218-229.

Pubmed: [Author and Title](#)
Google Scholar: [Author Only Title Only Author and Title](#)

McGurn, L.D., Moazami-Goudarzi, M., White, S.A., Suwal, T., Brar, B., Tang, J.Q., Espie, G.S., and Kimber, M.S. (2016). The structure, kinetics and interactions of the beta-carboxysomal beta-carbonic anhydrase, CcaA. Biochem J 473, 4559-4572.

Pubmed: [Author and Title](#)
Google Scholar: [Author Only Title Only Author and Title](#)

McKay, R.M., Gibbs, S., and Espie, G. (1993). Effect of dissolved inorganic carbon on the expression of carboxysomes, localization of Rubisco and the mode of inorganic carbon transport in cells of the cyanobacterium *Synechococcus* UTEX 625. Archives Microbiol 159, 21-29.

Pubmed: [Author and Title](#)
Google Scholar: [Author Only Title Only Author and Title](#)

Menon, B.B., Dou, Z., Heinhorst, S., Shively, J.M., and Cannon, G.C. (2008). *Halothiobacillus neapolitanus* carboxysomes sequester

heterologous and chimeric RubisCO species. PLoS One 3, e3570.

Pubmed: [Author and Title](#)

Google Scholar: [Author Only Title Only Author and Title](#)

Miller, H., Zhou, Z., Wollman, A.J., and Leake, M.C. (2015). Superresolution imaging of single DNA molecules using stochastic photoblinking of minor groove and intercalating dyes. Methods 88, 81-88.

Pubmed: [Author and Title](#)

Google Scholar: [Author Only Title Only Author and Title](#)

Miller, H., Cosgrove, J., Wollman, A.J.M., Taylor, E., Zhou, Z., O'Toole, P.J., Coles, M.C., and Leake, M.C. (2018). High-speed single-molecule tracking of CXCL13 in the B-follicle. Front Immunol 9, 1073.

Pubmed: [Author and Title](#)

Google Scholar: [Author Only Title Only Author and Title](#)

Niederhuber, M.J., Lambert, T.J., Yapp, C., Silver, P.A., and Polka, J.K. (2017). Superresolution microscopy of the beta-carboxysome reveals a homogeneous matrix. Mol Biol Cell 28, 2734-2745.

Pubmed: [Author and Title](#)

Google Scholar: [Author Only Title Only Author and Title](#)

Occhialini, A., Lin, M.T., Andralojc, P.J., Hanson, M.R., and Parry, M.A. (2016). Transgenic tobacco plants with improved cyanobacterial Rubisco expression but no extra assembly factors grow at near wild-type rates if provided with elevated CO₂. Plant J 85, 148-160.

Pubmed: [Author and Title](#)

Google Scholar: [Author Only Title Only Author and Title](#)

Plank, M., Wadhams, G.H., and Leake, M.C. (2009). Millisecond timescale slimfield imaging and automated quantification of single fluorescent protein molecules for use in probing complex biological processes. Integr Biol (Camb) 1, 602-612.

Pubmed: [Author and Title](#)

Google Scholar: [Author Only Title Only Author and Title](#)

Price, G.D., and Badger, M.R. (1991). Evidence for the role of carboxysomes in the cyanobacterial CO₂-concentrating mechanism. Can J Bot 69, 963-973.

Pubmed: [Author and Title](#)

Google Scholar: [Author Only Title Only Author and Title](#)

Rae, B.D., Long, B.M., Badger, M.R., and Price, G.D. (2012). Structural determinants of the outer shell of beta-carboxysomes in *Synechococcus elongatus* PCC 7942: roles for CcmK2, K3-K4, CcmO, and CcmL. PLoS One 7, e43871.

Pubmed: [Author and Title](#)

Google Scholar: [Author Only Title Only Author and Title](#)

Rae, B.D., Long, B.M., Badger, M.R., and Price, G.D. (2013). Functions, compositions, and evolution of the two types of carboxysomes: polyhedral microcompartments that facilitate CO₂ fixation in cyanobacteria and some proteobacteria. Microbiol Mol Biol Rev 77, 357-379.

Pubmed: [Author and Title](#)

Google Scholar: [Author Only Title Only Author and Title](#)

Reyes-Lamothe, R., Sherratt, D.J., and Leake, M.C. (2010). Stoichiometry and architecture of active DNA replication machinery in *Escherichia coli*. Science 328, 498-501.

Pubmed: [Author and Title](#)

Google Scholar: [Author Only Title Only Author and Title](#)

Ringgaard, S., van Zon, J., Howard, M., and Gerdes, K. (2009). Movement and equipositioning of plasmids by ParA filament disassembly. Proc Natl Acad Sci U S A 106, 19369-19374.

Pubmed: [Author and Title](#)

Google Scholar: [Author Only Title Only Author and Title](#)

Robson, A., Burrage, K., and Leake, M.C. (2013). Inferring diffusion in single live cells at the single-molecule level. Philos Trans R Soc Lond B Biol Sci 368, 20120029.

Pubmed: [Author and Title](#)

Google Scholar: [Author Only Title Only Author and Title](#)

Roivainen, M., Piirainen, L., Rysa, T., Narvanen, A., and Hovi, T. (1993). An immunodominant N-terminal region of VP1 protein of poliovirus that is buried in crystal structure can be exposed in solution. Virology 195, 762-765.

Pubmed: [Author and Title](#)

Google Scholar: [Author Only Title Only Author and Title](#)

Ryan, P., Forrester, T.J.B., Wroblewski, C., Kenney, T.M.G., Kitova, E.N., Klassen, J.S., and Kimber, M.S. (2018). The small RbcS-like domains of the beta-carboxysome structural protein, CcmM, bind RubisCO at a site distinct from that binding the RbcS subunit. J Biol Chem

Pubmed: [Author and Title](#)

Google Scholar: [Author Only Title Only Author and Title](#)

Saschenbrecker, S., Bracher, A., Rao, K.V., Rao, B.V., Hartl, F.U., and Hayer-Hartl, M. (2007). Structure and function of RbcX, an assembly chaperone for hexadecameric Rubisco. Cell 129, 1189-1200.

Pubmed: [Author and Title](#)

Google Scholar: [Author Only](#) [Title Only](#) [Author and Title](#)

Savage, D.F., Afonso, B., Chen, A.H., and Silver, P.A. (2010). Spatially ordered dynamics of the bacterial carbon fixation machinery. *Science* 327, 1258-1261.

Pubmed: [Author and Title](#)

Google Scholar: [Author Only](#) [Title Only](#) [Author and Title](#)

Sbalzarini, I.F., and Koumoutsakos, P. (2005). Feature point tracking and trajectory analysis for video imaging in cell biology. *J Struct Biol* 151, 182-195.

Pubmed: [Author and Title](#)

Google Scholar: [Author Only](#) [Title Only](#) [Author and Title](#)

Schwarz, D., Nodop, A., Hüge, J., Purfurst, S., Forchhammer, K., Michel, K.P., Bauwe, H., Kopka, J., and Hagemann, M. (2011). Metabolic and transcriptomic phenotyping of inorganic carbon acclimation in the cyanobacterium *Synechococcus elongatus* PCC 7942. *Plant Physiol* 155, 1640-1655.

Pubmed: [Author and Title](#)

Google Scholar: [Author Only](#) [Title Only](#) [Author and Title](#)

Shashkova, S., and Leake, M.C. (2017). Single-molecule fluorescence microscopy review: shedding new light on old problems. *Biosci Rep* 37.

Pubmed: [Author and Title](#)

Google Scholar: [Author Only](#) [Title Only](#) [Author and Title](#)

Shashkova, S., Wollman, A.J., Hohmann, S., and Leake, M.C. (2018). Characterising maturation of GFP and mCherry of genomically integrated fusions in *Saccharomyces cerevisiae*. *Bio Protoc* 8, e2710.

Pubmed: [Author and Title](#)

Google Scholar: [Author Only](#) [Title Only](#) [Author and Title](#)

Shively, J.M., Ball, F.L., and Kline, B.W. (1973). Electron microscopy of the carboxysomes (polyhedral bodies) of *Thiobacillus neapolitanus*. *J Bacteriol* 116, 1405-1411.

Pubmed: [Author and Title](#)

Google Scholar: [Author Only](#) [Title Only](#) [Author and Title](#)

Sommer, M., Cai, F., Melnicki, M., and Kerfeld, C.A. (2017). β -Carboxysome bioinformatics: identification and evolution of new bacterial microcompartment protein gene classes and core locus constraints. *J Exp Bot* 68, 3841-3855.

Pubmed: [Author and Title](#)

Google Scholar: [Author Only](#) [Title Only](#) [Author and Title](#)

Sommer, M., Sutter, M., Gupta, S., Kirst, H., Turmo, A., Lechno-Yossef, S., Burton, R.L., Saechao, C., Sloan, N.B., Cheng, X., Chan, L.G., Petzold, C.J., Fuentes-Cabrera, M., Ralston, C.Y., and Kerfeld, C.A. (2019). Heterohexamers formed by CcmK3 and CcmK4 increase the complexity of beta carboxysome Shells. *Plant Physiol* 179, 156-167.

Pubmed: [Author and Title](#)

Google Scholar: [Author Only](#) [Title Only](#) [Author and Title](#)

Stracy, M., Wollman, A.J., Kaja, E., Gapinski, J., Lee, J.E., Leek, V.A., McKie, S.J., Mitchenall, L.A., Maxwell, A., Sherratt, D.J., Leake, M.C., and Zawadzki, P. (2018). Single-molecule imaging of DNA gyrase activity in living *Escherichia coli*. *Nucleic Acids Res* 47, 210-220.

Pubmed: [Author and Title](#)

Google Scholar: [Author Only](#) [Title Only](#) [Author and Title](#)

Sun, Y., Casella, S., Fang, Y., Huang, F., Faulkner, M., Barrett, S., and Liu, L.N. (2016). Light modulates the biosynthesis and organization of cyanobacterial carbon fixation machinery through photosynthetic electron flow. *Plant Physiol* 171, 530-541.

Pubmed: [Author and Title](#)

Google Scholar: [Author Only](#) [Title Only](#) [Author and Title](#)

Sutter, M., Faulkner, M., Aussignargues, C., Paasch, B.C., Barrett, S., Kerfeld, C.A., and Liu, L.-N. (2016). Visualization of bacterial microcompartment facet assembly using high-speed atomic force microscopy. *Nano Letters* 16, 1590-1595.

Pubmed: [Author and Title](#)

Google Scholar: [Author Only](#) [Title Only](#) [Author and Title](#)

Tanaka, S., Sawaya, M.R., Kerfeld, C.A., and Yeates, T.O. (2007). Structure of the RuBisCO chaperone RbcX from *Synechocystis* sp. PCC6803. *Acta crystallographica. Section D, Biological crystallography* 63, 1109-1112.

Pubmed: [Author and Title](#)

Google Scholar: [Author Only](#) [Title Only](#) [Author and Title](#)

Tanaka, S., Kerfeld, C.A., Sawaya, M.R., Cai, F., Heinhorst, S., Cannon, G.C., and Yeates, T.O. (2008). Atomic-level models of the bacterial carboxysome shell. *Science* 319, 1083-1086.

Pubmed: [Author and Title](#)

Google Scholar: [Author Only](#) [Title Only](#) [Author and Title](#)

Tinevez, J.-Y., Perry, N., Schindelin, J., Hoopes, G.M., Reynolds, G.D., Laplantine, E., Bednarek, S.Y., Shorte, S.L., and Eliceiri, K.W. (2017). TrackMate: An open and extensible platform for single-particle tracking. *Methods* 115, 80-90.

Pubmed: [Author and Title](#)

Google Scholar: [Author Only](#) [Title Only](#) [Author and Title](#)

Vecchiarelli, A.G., Hwang, L.C., and Mizuuchi, K. (2013). Cell-free study of F plasmid partition provides evidence for cargo transport by

a diffusion-ratchet mechanism. Proc Natl Acad Sci U S A 110, E1390-1397.

Pubmed: [Author and Title](#)

Google Scholar: [Author Only](#) [Title Only](#) [Author and Title](#)

Wang, H., Yan, X., Aigner, H., Bracher, A., Nguyen, N.D., Hee, W.Y., Long, B.M., Price, G.D., Hartl, F.U., and Hayer-Hartl, M. (2019). Rubisco condensate formation by CcmM in beta-carboxysome biogenesis. Nature 566, 131-135.

Pubmed: [Author and Title](#)

Google Scholar: [Author Only](#) [Title Only](#) [Author and Title](#)

Whitehead, L., Long, B.M., Price, G.D., and Badger, M.R. (2014). Comparing the in vivo function of alpha-carboxysomes and beta-carboxysomes in two model cyanobacteria. Plant Physiol 165, 398-411.

Pubmed: [Author and Title](#)

Google Scholar: [Author Only](#) [Title Only](#) [Author and Title](#)

Wollman, A.J., and Leake, M.C. (2015). Millisecond single-molecule localization microscopy combined with convolution analysis and automated image segmentation to determine protein concentrations in complexly structured, functional cells, one cell at a time. Faraday Discuss 184, 401-424.

Pubmed: [Author and Title](#)

Google Scholar: [Author Only](#) [Title Only](#) [Author and Title](#)

Wollman, A.J., and Leake, M.C. (2016). Single-molecule narrow-field microscopy of protein-DNA binding dynamics in glucose signal transduction of live yeast cells. Methods Mol Biol 1431, 5-15.

Pubmed: [Author and Title](#)

Google Scholar: [Author Only](#) [Title Only](#) [Author and Title](#)

Wollman, A.J., Miller, H., Foster, S., and Leake, M.C. (2016a). An automated image analysis framework for segmentation and division plane detection of single live Staphylococcus aureus cells which can operate at millisecond sampling time scales using bespoke Slimfield microscopy. Physical Biol 13, 055002.

Pubmed: [Author and Title](#)

Google Scholar: [Author Only](#) [Title Only](#) [Author and Title](#)

Wollman, A.J., Syeda, A.H., McGlynn, P., and Leake, M.C. (2016b). Single-molecule observation of DNA replication repair pathways in E. coli. Adv Exp Med Biol 915, 5-16.

Pubmed: [Author and Title](#)

Google Scholar: [Author Only](#) [Title Only](#) [Author and Title](#)

Wollman, A.J., Shashkova, S., Hedlund, E.G., Friemann, R., Hohmann, S., and Leake, M.C. (2017). Transcription factor clusters regulate genes in eukaryotic cells. eLife 6, e27451.

Pubmed: [Author and Title](#)

Google Scholar: [Author Only](#) [Title Only](#) [Author and Title](#)

Woodger, F.J., Badger, M.R., and Price, G.D. (2003). Inorganic carbon limitation induces transcripts encoding components of the CO₂-concentrating mechanism in Synechococcus sp. PCC7942 through a redox-independent pathway. Plant Physiol 133, 2069-2080.

Pubmed: [Author and Title](#)

Google Scholar: [Author Only](#) [Title Only](#) [Author and Title](#)

Yeates, T.O., Crowley, C.S., and Tanaka, S. (2010). Bacterial microcompartment organelles: protein shell structure and evolution. Annual Rev Biophys 39, 185-205.

Pubmed: [Author and Title](#)

Google Scholar: [Author Only](#) [Title Only](#) [Author and Title](#)